Key Points:
- Seaglider surveys at Station Papa (50°N, 145°W) resolved mesoscale gradients and circulation June 2008 to January 2010
- Surveys revealed anomalous westward flow, thermohaline fine structure, and two distinct water masses in the halocline
- These phenomena were due to an anticyclonic meander of the North Pacific Current near OSP

Seaglider surveys at Ocean Station Papa: Circulation and water mass properties in a meander of the North Pacific Current

Noel A. Pelland[1,2], Charles C. Eriksen[1], and Meghan F. Cronin[3]

[1]School of Oceanography, University of Washington, Seattle, Washington, USA, [2]Now at NOAA Alaska Fisheries Science Center, and University of Washington Joint Institute for the Study of the Atmosphere and Ocean, Seattle, Washington, USA, [3]NOAA Pacific Marine Environmental Laboratory, Seattle, Washington, USA

Abstract A Seaglider autonomous underwater vehicle augmented the Ocean Station Papa (OSP; 50°N, 145°W) surface mooring, measuring spatial structure on scales relevant to the monthly evolution of the moored time series. During each of three missions from June 2008 to January 2010, a Seaglider made biweekly 50 km × 50 km surveys in a bowtie-shaped survey track. Horizontal temperature and salinity gradients measured by these surveys were an order of magnitude stronger than climatological values and sometimes of opposite sign. Geostrophically inferred circulation was corroborated by moored acoustic Doppler current profiler measurements and AVISO satellite altimetry estimates of surface currents, confirming that glider surveys accurately resolved monthly scale mesoscale spatial structure. In contrast to climatological North Pacific Current circulation, upper-ocean flow was modestly northward during the first half of the 18 month survey period, and weakly westward during its latter half, with Rossby number $\mathcal{O}(0.01)$. This change in circulation coincided with a shift from cool and fresh to warm, saline, oxygen-rich water in the upper-ocean halocline, and an increase in vertical fine structure there and in the lower pycnocline. The anomalous flow and abrupt water mass transition were due to the slow growth of an anticyclonic meander within the North Pacific Current with radius comparable to the scale of the survey pattern, originating to the southeast of OSP.

1. Introduction

The southern Gulf of Alaska (GOA) in the northeast Pacific Ocean is the site of one of the longest and highest-quality records of open ocean measurements in the world, the Ocean Station Papa (OSP) time series (50°N, 145°W) [*Freeland*, 2007]. Ocean Station Papa lies at the southern edge of the cyclonic GOA (northeast Pacific subpolar) gyre (Figure 1), which is bounded to the east by the North American coast, to the north and west by the coast of Alaska, and to the south by the broad, eastward-flowing Subarctic Current/North Pacific Current (NPC) that forms the boundary between the GOA and the adjacent anticyclonic northeast Pacific subtropical gyre [*Tabata*, 1965; *Freeland and Cummins*, 2005; *Cummins and Freeland*, 2007; *Whitney et al.*, 2007]. Currents are weak near OSP in the low-energy GOA, though mesoscale eddies and meanders are nevertheless ubiquitous, and the ratio of eddy kinetic energy to mean kinetic energy in the eastern GOA is comparable to other regions in the North Pacific Ocean [*Thomson et al.*, 1990; *Paduan and Niiler*, 1993]. Eddies formed from instabilities or flow-topography interaction along the North American continental margin transport coastal water and associated nutrient, heat, and freshwater signatures seaward away from the eastern gyre boundary [e.g., *Crawford et al.*, 2005; *Pelland et al.*, 2013; *Lyman and Johnson*, 2015], but likely do not account for all of the eddying motions in the gyre interior [*Thomson et al.*, 1990; *Chelton et al.*, 2011].

The weak circulation at OSP, combined with the extensive duration and quality of its oceanographic record, has made it an attractive natural laboratory for the study of boundary layer dynamics, transfer of kinetic energy between atmosphere and ocean in midlatitudes, surface gas exchange, and the biological carbon pump [e.g., *Davis et al.*, 1981a,1981b; *Large et al.*, 1986; *Paduan and deSzoeke*, 1986; *Emerson*, 1987; *Thomas et al.*, 1990; *Large and Crawford*, 1995; *D'Asaro et al.*, 1995; *Wong et al.*, 2002; *Steiner et al.*, 2007; *Emerson and Stump*, 2010; *Vagle et al.*, 2010; *Dohan and Davis*, 2011; *Alford et al.*, 2012]. In addition, the many years of shipboard measurements have also characterized the annual cycle at OSP well [*Tabata*, 1965; *Large*, 1996; *Whitney and Freeland*, 1999], which has made it an important location for development and testing of one-dimensional numerical models, and their ability to replicate the seasonal cycle of upper-ocean structure
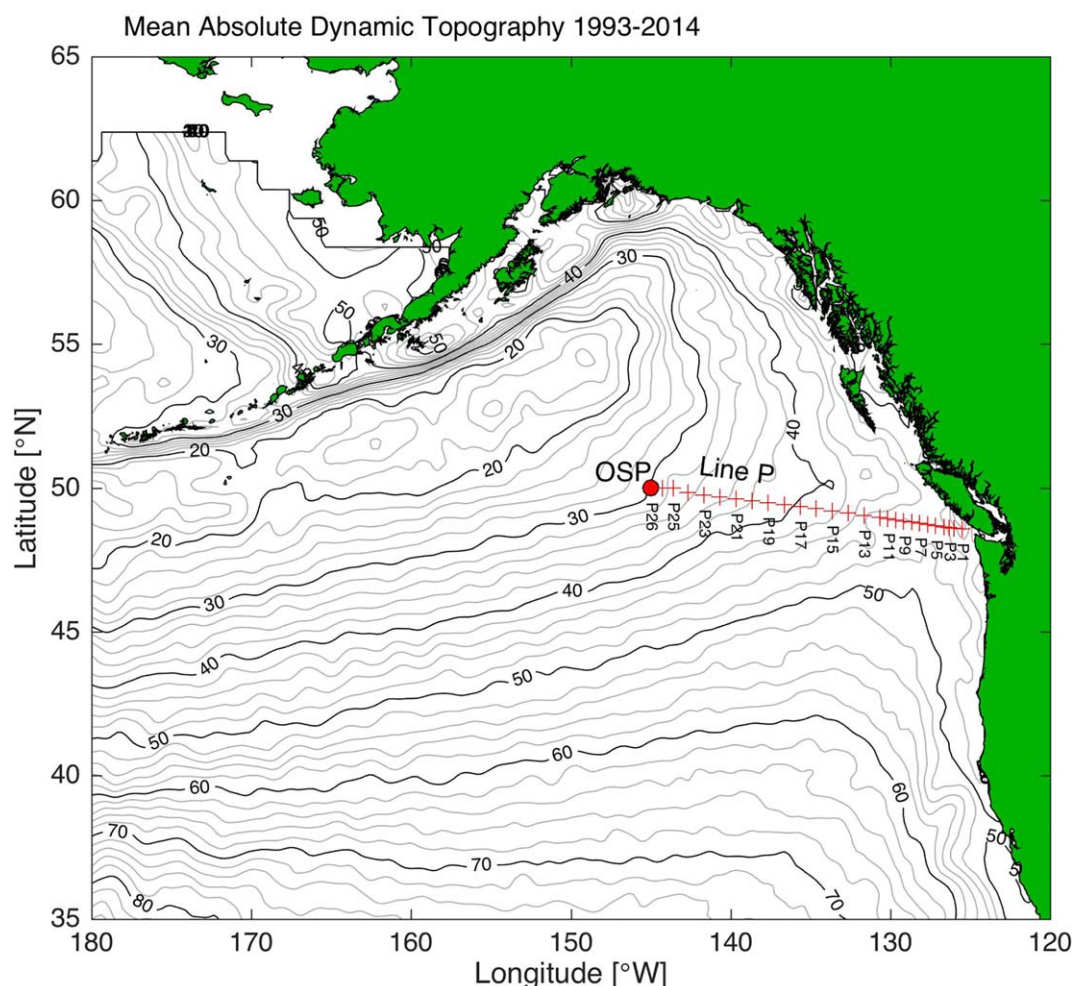
Figure 1. Sea surface mean dynamic topography (cm of sea surface height) used by AVISO in the Absolute Dynamic Topography all-satellite gridded product. Contour interval is 2 cm. Red crosses indicate hydrographic stations that compose Line P. For clarity, only every second station is labeled. Red circle at 50°N, 145°W highlights station P26, also known as Ocean Station Papa (OSP). The center of the Gulf of Alaska gyre is visible as a relative low in sea surface height to the northwest of OSP. The North Pacific Current is evident as a wide swath of east-northeastward flow that approaches the North American coastal regions at latitudes 35°N–50°N. OSP lies near the northern edge of this current.

based on atmospheric inputs of heat, freshwater, and momentum [*Denman and Miyake*, 1973; *Davis et al.*, 1981b; *Martin*, 1985; *Gaspar*, 1988; *Archer et al.*, 1993; *Large et al.*, 1994; *Large*, 1996; *McClain et al.*, 1996; *Jackson et al.*, 2009; *Thomson and Fine*, 2009].

As with other ocean time series sites, OSP has also been a test bed and proving ground for new technologies and observing strategies. Continuing this progression, beginning in June 2007, OSP has been the site of a well-instrumented NOAA surface mooring [*Emerson and Stump*, 2010; *Hamme et al.*, 2010; *Emerson et al.*, 2011; *Cronin et al.*, 2012, 2015; Fassbender et al., 2016]. Two upward-looking ADCP moorings were also deployed in 2008 and 2009 [*Alford et al.*, 2012] and a surface Waverider buoy starting in June 2010 [*Thomson et al.*, 2013]. From June 2008 to January 2010, the mooring array was augmented by three successive Seaglider autonomous underwater vehicle missions, where each vehicle repeatedly followed a bowtie-shaped survey track inscribed within a 50 km × 50 km square region. The results of these surveys are the focus of this present study.

Seaglider surveys represent an observational milestone for OSP, in that individual vehicles provided continuous estimates of the horizontal gradients of temperature, salinity, and dissolved oxygen in the top 1000 m in the region surrounding the mooring, along with well-resolved vertical profiles of these quantities over the course of 18 successive months. Measurement of horizontal gradients allows the estimation of vertical

geostrophic shear and horizontal advection, thus potentially improving the ability to resolve the balances of physical and biogeochemical tracers at OSP. Previously, mesoscale upper-ocean horizontal gradients of temperature and salinity had been collected near OSP either from individual shipboard surveys, drifting buoy, and moored deployments with maximum duration of a few months [*Large et al.*, 1986; *Paduan and Niiler*, 1993; *Matear*, 1993; *Torruella*, 1995] or from the Argo array, which persistently samples large-scale circulation features but is spatially too coarse to describe mesoscale eddies [*Ren and Riser*, 2009]. The Seaglider time series described here builds upon these previous observational efforts and also serves as an important precursor to ongoing mooring-glider time series deployed at OSP beginning in 2013 as part of the National Science Foundation-supported Ocean Observatories Initiative (OOI; http://www.whoi.edu/ooi_cgsn/station-papa).

The principal objectives of Seaglider deployments at OSP were twofold: (1) to resolve horizontal gradients through the top kilometer of the oceanic water column to estimate absolute geostrophic current and horizontal tracer advection, and (2) to estimate vertical advection and diffusion in order to describe the evolution of heat, freshwater, and dissolved oxygen. Here the horizontal gradients, estimates of absolute geostrophic current, and associated water mass properties are described, while application of these to the remaining objectives appears in forthcoming contributions and in *Pelland* [2015].

Following this introduction, section 2 describes the data sources and methods used in the study. Section 3 provides a brief review of upper-ocean structure at OSP and describes the estimated geostrophic circulation and water mass properties. Section 4 discusses these results and evaluates possible origins of the phenomena observed at OSP in 2008–2010, and conclusions follow in section 5.

2. Data and Methods

2.1. Moored Array

The NOAA Ocean Climate Stations (OCS) installation at OSP consists of a single taut-line mooring with sensors designed to sample atmospheric properties, mixed layer properties, and temperature T and salinity S profiles in the top 300 m. Beginning in summer 2007, the mooring has been deployed and recovered in June of each year from the CCGS *John P. Tully* in cooperation with the Canadian Coast Guard and the Department of Fisheries and Oceans Canada (DFO) Institute of Ocean Sciences (IOS) during their sampling of Line P, a set of oceanographic stations established between the Strait of Juan de Fuca entrance and OSP [*Freeland*, 2007, Figure 1]. The mooring location alternates each year between two sites near OSP. In deployments beginning in odd-numbered years, the target mooring site is 50°08′N, 144°50′W, while in even years it is to the southwest at 50°03′N, 144°53′W (Figure 2a). The taut line results in a watch circle radius of 1.25 km and maximum displacement from the nominal position of 8 km over the course of the time series to date. During the overlap period with Seaglider surveys, the mooring surface buoy broke free on 11 November 2008. High-resolution postprocessed surface data and telemetered daily average subsurface data are available from the start of Seaglider time series on 8 June 2008 until mooring break. No mooring data are available from 11 November 2008 until deployment of the successor mooring on 14 June 2009 (Figure 2c). All available moored data were obtained from the NOAA OCS group (http://www.pmel.noaa.gov/ocs/).

The buoy atmospheric measurements include wind speed and direction, air temperature, relative humidity, barometric pressure, and short-wave and long-wave radiation and rain rate. The buoy also samples sea-surface temperature and salinity at 1.2 m depth. Atmospheric measurements and estimates of surface fluxes are described in further detail in *Cronin et al.* [2015]. Subsurface measurements along the OSP mooring line include observations of T, S, and vector current meter measurements of eastward u and northward v velocity components at multiple depths. In 2009, during overlap with the Seaglider time series, T was measured at 16 depths from the surface to 300 m (1.2, 5, 10, 20, 25, 30, 36, 45, 60, 80, 100, 120, 150, 175, 200, and 300 m), and S was measured at 13 depths from the surface to 200 m (1.2, 10, 20, 25, 30, 36, 45, 60, 80, 100, 120, 150, and 200 m). T and S were sampled using sensors from Sea-Bird Electronics (SBE), including the SBE-39 (T accuracy $\pm0.002°C$), SBE-37 MicroCAT ($T\pm0.003°C$, $S\pm0.02$), and SBE-51 ($T\pm0.005°C$, $S\pm0.02$), or in two instances (150 and 200 m depth in 2009), PMEL ATLAS modules. The ATLAS module has a T accuracy of $\pm0.02°C$ and S accuracy ±0.02 (http://www.pmel.noaa.gov/ocs/sensors). In the mooring deployment beginning 2009, an RD Instruments (RDI) Doppler Volume Sampler current meter, with accuracy bounds of $1.0\% \pm 0.5$ cm s^{-1}, sampled horizontal velocity at 35 m depth.
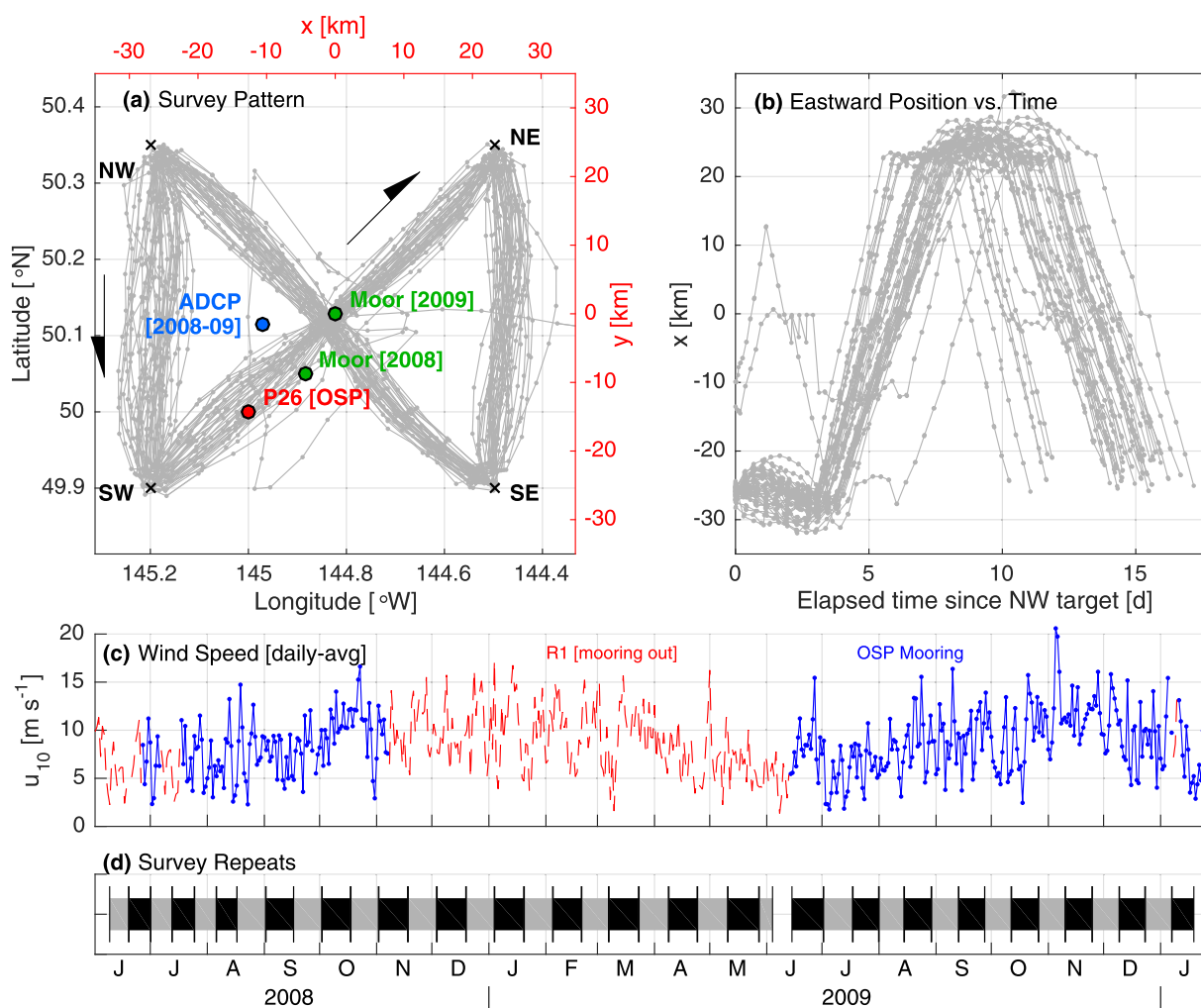
Figure 2. Seaglider surveys at Ocean Station Papa (OSP), overview. (a) Survey pattern; gray curve indicates Seaglider track, gray dots give descent-ascent cycle center points. Arrows indicate direction of survey. Green dots are NOAA surface mooring locations in 2008/2009 deployment years. Blue dot indicates subsurface ADCP mooring location in 2009 deployment year; this mooring was located at OSP in 2008. (b) The eastward distance of gliders relative to the center of the survey pattern, as a function of time since the initiation near survey target NW of each repeat cycle of the survey. (c) Daily average 10 m wind speed from the OSP mooring (blue curve) or NCEP/NCAR Reanalysis 1 (R1) product (red dashed curve). The mooring was absent from OSP 11 November 2008 to 14 June 2009. (d) Survey repeats (alternating gray/black) versus time; vertical lines indicate the times at which the glider achieved the northwest (NW) target location.

This study also employs data from a subsurface ADCP mooring deployed near OSP during June 2008 to June 2010 [*Alford et al.*, 2012], locations of which are indicated in Figure 2a. During both years, an RDI 75 kHZ Long-Ranger upward-looking unit was mounted at 800 m, giving ensemble velocity profiles in 16 m vertical bins every 30 min. A second upward-looking, higher-frequency unit was mounted at 130 m from June 2008 (300 kHz RDI Sentinel) and 200 m (150 kHz RDI Quartermaster) from June 2009 onward. These units estimated ensemble profiles in 4 m vertical bins also every 30 min. The top 10% of the upper unit profile was discarded due to sidelobe contamination. Weak acoustic scattering levels led to large gaps in the upper instrument record during the second year, extending up to 100 m depth from the surface [*Alford et al.*, 2012].

2.2. Seaglider Surveys and Processing

Two Seagliders [*Eriksen et al.*, 2001] were deployed individually at OSP in three consecutive missions. Seaglider (SG) 144 was deployed from 8 June to 30 August 2008 (data available at http://accession.nodc.noaa.gov/0155762), SG120 from 30 August 2008 to 14 June 2009 (http://accession.nodc.noaa.gov/0155598), and SG144 again from 14 June 2009 to 18 January 2010 (http://accession.nodc.noaa.gov/0155879). SG120 ceased sampling due to a low battery state on 4 June 2009, hence there was a 10 day gap in sampling prior to the deployment of SG144 by the CCGS *Tully* on 14 June. On 18 January 2010, SG144 departed OSP and

proceeded inshore along Line P until 2 April, after which it was recovered near station P6 (Figure 1) approximately 160 km from the inshore terminus of Line P.

The Seagliders profiled from the surface to 1000 m and back in a series of dive-climb cycles, using a buoyancy engine to travel with cycle-average horizontal speeds of 21.3 ± 3.2 cm s^{-1} (mean $\pm$ standard deviation across all cycles) through the water along a typical 3:1 horizontal:vertical glide slope. Seagliders at OSP proceeded through a series of five targets arranged in a "bowtie" pattern inscribed in a 50 km $\times$ 50 km box centered on the 2009 mooring site (Figure 2a), similar to that of surveys previously conducted at the Station A Long-Term Oligotrophic Habitat Assessment portion of the Hawaii Ocean Time Series [*Nicholson et al.*, 2008; *Emerson et al.*, 2008]. Vehicles proceeded through the targets in the order NW-SW-NE-SE-NW and repeated this pattern on average once every 14.5 days, resulting in 38 complete and two partial circuits during the survey time series (Figures 2a, 2b, and 2d). Seagliders executed 36–59 dive-climb cycles during each survey circuit (median 43). A total of 1693 cycles were performed (3386 profiles collected) between 8 June 2008 and SG144's departure on 18 January 2010. An additional 219 cycles were performed by SG144 during its transit along Line P.

Each vehicle was equipped with a thermistor and conductivity cell, identical to those used on SBE-3 and SBE-4 instruments, mounted within a cylindrical duct atop a dorsal sting. Custom SBE circuits designed to stabilize rapidly after power application were used to produce frequency outputs for temperature and conductivity, as with SBE-3 and SBE-4 instruments. These sensor packages were calibrated by SBE before and after each OSP deployment. In these and most Seaglider configurations, flow through the conductivity cell and past the thermistor is not pumped and instead induced by flow past the vehicle as it glides. For salinity calculations, in which the thermal contribution to conductivity must be estimated, corrections were applied for position differences between the thermistor and conductivity cell and thermal inertia of the conductivity cell as summarized in *Pelland et al.* [2013]. Briefly, these corrections require an estimate of the flow speed through the conductivity cell, which depends on vehicle speed. Estimates of vehicle speed, made using the steady flight equations of *Eriksen et al.* [2001], depend on vehicle buoyancy, which is itself a function of water density and salinity. An iterative procedure is used to apply these salinity corrections on each dive-climb cycle. From an initial guess of vehicle velocity, salinity corrections at each sample are first determined using the solutions of C. C. Eriksen (unpublished manuscript, 2016) for Seaglider conductivity cell thermal response under flushing by the vehicle flow. The initial salinity corrections yield a corrected buoyancy at each sample, which in turn yields updated estimates of vehicle speed, and thereby a second set of salinity corrections. This process was repeated through several loops until convergence. Remaining spikes or obvious visual errors due to vehicle stalls or temporary fouling of the conductivity cell were removed.

Following these corrections, systematic S errors were evident in the stratified layer immediately deeper than the surface mixed layer (defined below), where the sensor sample rate was insufficient to resolve the conductivity cell thermal response within strong thermal stratification. The errors were evident as excursions in T-S that did not match profiles from the CCGS *Tully*. These were corrected by exploiting the nearly linear T-S relation that extends through the thermal stratification that is present at the base of the mixed layer [*Tabata*, 1965; *D'Asaro*, 1985; *Paduan and deSzoeke*, 1986]. For profiles June 2008 to January 2009 and June 2009 to January 2010, S was interpolated as a function of T between shallow and deep "anchor" points, respectively, located in the mixed layer and in stratified water deeper than the mixed layer. These points were chosen to be in regions of weak thermal stratification and hence reliable S samples (see the supporting information [SI]). This procedure was applied to 2638 of 3386 Seaglider profiles at OSP; the mean depth extent in which S was interpolated in these profiles was 37.8 m (average upper boundary depth of 34.5 m, lower boundary 72.3 m). Further details of this procedure are included in the SI.

Where necessary, offsets were applied to measurements of conductivity in order to give better agreement between deep T-S measurements from Seagliders and those collected from Conductivity-Temperature-Depth (CTD) casts performed by the CCGS *Tully* [*Pelland*, 2015]. Following these adjustments, the mean offset in deep salinity between CCGS *Tully* and Seaglider measurements was, respectively, -0.0010, 0.0007, and -0.0029 for the first, second, and third deployments. Following the above corrections, Seaglider S samples are considered to have accuracy ± 0.03 and T samples ± 0.003°C. Where interpolation as a function of T was performed, S accuracy is estimated to have absolute bounds ± 0.08 and 95% bounds of ± 0.03 (SI).

Each vehicle was also equipped with a Western Environmental Technologies (WET) Laboratories ECO-BB2F "puck"-style sensor, sampling optical backscatter on two wavelengths and fluorescence on a single

wavelength, and two dissolved oxygen sensors, an SBE-43 Clark-type sensor and an Aanderaa Instruments 3830 oxygen optode. Only the optode samples are discussed here. These were adjusted to match Winkler titration measurements collected from the CCGS *Tully* and R/V *Thomas G. Thompson* [*Pelland*, 2015]. Optode samples are presented on isopycnals within the halocline at OSP (defined below). In this layer of steep vertical oxygen gradients, the slow instrument response time results in a 10–15 μmol kg^{-1} positive (negative) bias in measurements of dissolved oxygen per unit mass [O$_2$] on descent (ascent) profiles. Measurements were cycle-averaged, then daily-averaged to reduce these errors. The resulting daily-average samples are considered accurate to within ± 3 μmol kg^{-1}.

With the exception of September 2008, Seaglider sample intervals for all instruments were 10 s while profiling from the surface to 80 m, 20 s from 80 to 150 m, 30 s from 150 to 300 m, and 60 s when profiling between 300 and 1000 m. Resultant mean vertical spacing between samples in each zone was, respectively, 0.93 m (0–80 m depth), 1.49 m (80–150 m), 2.30 m (150–300 m), and 4.17 m (300–1000 m). All scalar variables including *T*, *S*, [O$_2$], in situ density ρ, potential temperature referenced to the sea surface θ, and potential density ρ_θ were bin-averaged in depth intervals of 2 m from the surface to 150 m, 5 m from 150 to 300 m, and 20 m at greater depths.

Samples of seawater density corrected for conductivity cell position and thermal inertia give an estimate of vehicle buoyancy and velocity through water at each sample point as described above. The difference between observed final displacement (climb end minus dive start location) and integrated displacement through water gives an estimate of time-averaged current experienced by the vehicle. This is equated to 0–1000 m depth-averaged current (DAC) since the vehicle vertical velocity is approximately constant throughout each cycle. Independent of errors induced by onboard compass calibration, DAC samples are considered accurate to within ~ 1 cm s^{-1} on each cycle [*Eriksen et al.*, 2001].

2.2.1. Estimates of Horizontal Gradients

In contrast to the OSP moored time series, the record of a scalar quantity sampled by Seagliders at a given depth reflects variability in both time and space. Least squares multivariable regression was used to estimate the contribution of spatial structure to the observed variability of scalar quantities along depth surfaces, in the process providing an estimate of the horizontal gradient of these quantities. An example of this procedure is described here for Seaglider samples of θ at 120 m depth in July 2008.

When plotted as a function of time, $\theta(z = -120\,\text{m})$ exhibits approximately fortnightly oscillations of amplitude $\sim 0.5^\circ$C in this month (Figure 3a). These oscillations are of a similar character to the time record of the glider eastward position relative to the survey pattern center, *x* (Figure 3b). Plotting $\theta(z = -120\,\text{m})$ in plan view during July 2008 reveals persistent spatial structure in which θ is elevated on the eastern side of the survey pattern (Figure 3c).

To quantify the horizontal gradient of θ, the 223 samples of $\theta(z = -120\,\text{m})$ in July 2008 were fit with a multivariable regression model that includes terms that are functions of *x*, *y*, and *t*:

$$\theta_k = A + Bx_k + Cy_k + Dt'_k + Et'^2_k + \epsilon_k = X\vec{a} + \vec{\epsilon} = \vec{\theta}, \tag{1}$$

where for sample *k* during the month ($k = 1, 2, \cdots, 223$), θ_k is the observed potential temperature, x_k and y_k are, respectively, eastward and northward distances from the center of the survey pattern, t'_k is the time since midmonth (day 15), and ϵ_k is the residual from the best fit. *X* is a 223-by-5 matrix of predictors, such that row *k* of *X* is $[1 \; x_k \; y_k \; t'_k \; t'^2_k]$, while $\vec{a} = [ABCDE]^\mathsf{T}$ is a vector of regression coefficients to be estimated, and superscript T indicates a matrix transpose. $\vec{\epsilon}$ is the 223-by-1 vector of residuals from the least squares fit, and $\vec{\theta} = [\theta_1 \; \theta_2 \; \cdots \; \theta_{223}]^\mathsf{T}$ is a 223-by-1 vector of samples of θ in this depth bin and month. The linear-space, quadratic-time form of (1) was chosen as the best compromise between data fitting and model complexity [*Pelland*, 2015]. Small-scale noise visible in Figures 3a and 3c, which is due in part to vertical displacement of isotherms by internal waves at time scales comparable to those of a glider cycle, prevents estimation of higher-order *x* and *y* terms.

The best fit coefficients are those that minimize the sum of square residuals; i.e.,

$$\vec{a} = (X^\mathsf{T} X)^{-1}(X^\mathsf{T} \vec{\theta}), \tag{2}$$

where superscript -1 indicates a matrix inverse. The best fit line from this regression $X\vec{a}$ is the dashed red line in Figure 3a. The best fit coefficient vector elements *B* and *C*, respectively, provide an estimate of the
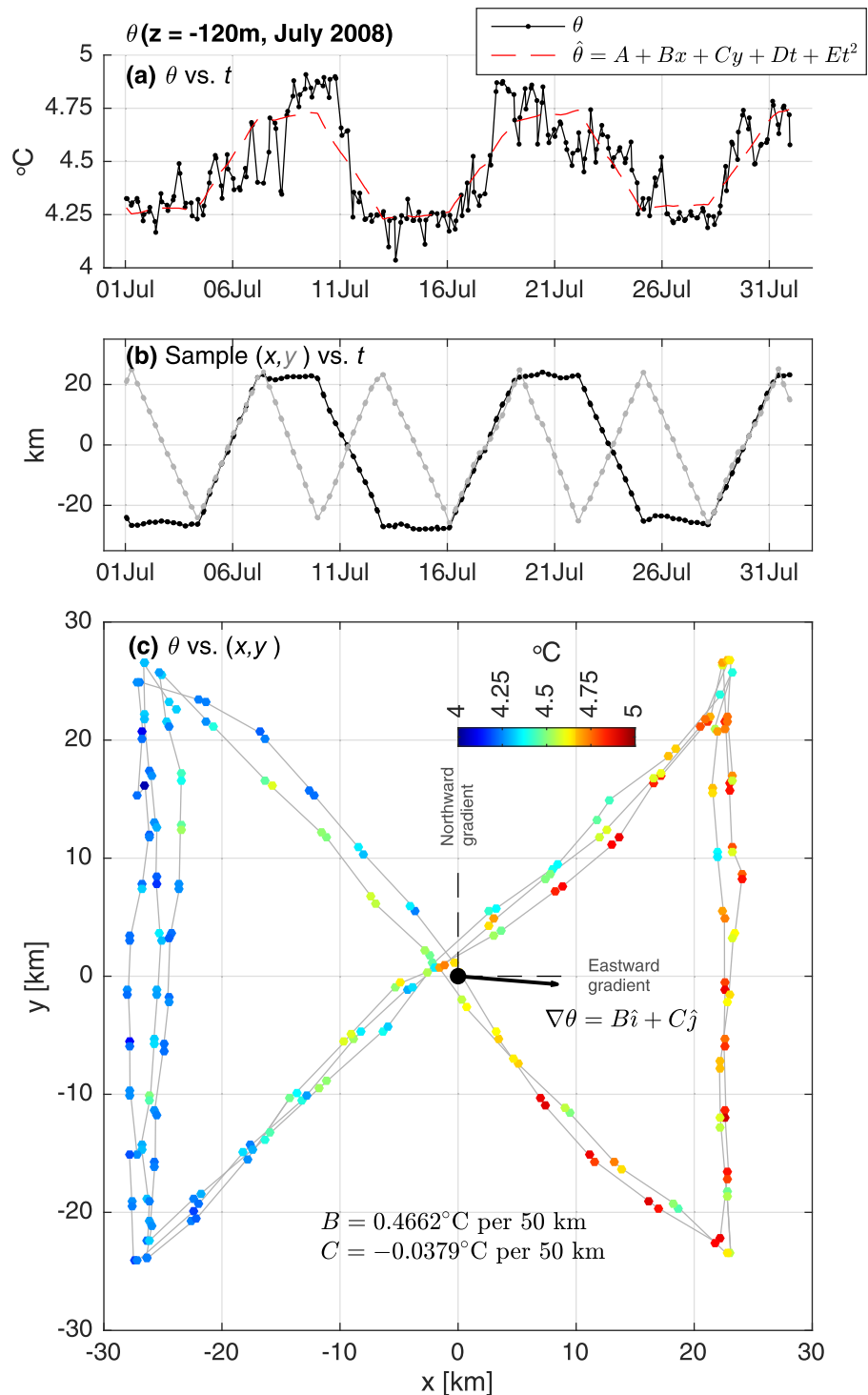
Figure 3. Example estimation of spatial gradient of potential temperature at 120 m depth $\theta(z=-120\,\text{m})$ during July 2008. In Figure 3a, black curve is Seaglider-observed θ versus time t, and red dashed curve is the best fit multivariable regression line $\hat{\theta}$ of the form (1). (b) Eastward x (black) and northward y (gray) coordinates of θ samples relative to the survey pattern center versus t. (c) Observed θ versus x and y, along with the estimated horizontal gradient (using coefficients from best fit line in Figure 3a), which is plotted as a black vector with its origin at the center of the survey pattern (scale: 10 km = 0.5°C per 50 km).

eastward ($\partial\theta/\partial x$) and northward ($\partial\theta/\partial y$) components of the horizontal gradient vector of θ at this depth ($\nabla\theta=(\partial\theta/\partial x)\hat{\imath}+(\partial\theta/\partial y)\hat{\jmath}$, where $\hat{\imath}$ and $\hat{\jmath}$ are, respectively, unit vectors in the x and y directions). The estimate of this vector using the best fit coefficients is plotted in Figure 3c with its origin at the center of the

track pattern. Its orientation indicates that the estimated horizontal gradient of θ at 120 m depth is almost entirely to the east, in agreement with the warmer temperatures on the eastern side of the survey pattern.

The least squares regression technique described above was used to construct estimates of the horizontal gradients of all scalar variables in each depth bin and calendar month. The procedure was slightly modified in the upper 100 m after June 2009 which will be described below. In all cases, estimates of horizontal gradients were constructed using regression fits to data selected in independent, monthly intervals; the first of these extends from 8 to 30 June 2008, the last from 1 to 21 January 2010, and all intervals between these two extend from the first to the last day of each month. The monthly interval duration corresponds to approximately the amount of time required for a Seaglider to perform two complete circuits of the bowtie survey track. This duration was chosen empirically as a compromise between a time scale long enough to allow surveys to fully resolve spatial structure, and short enough to avoid unnecessarily smearing over changes associated with mesoscale flow at OSP. Visually, spatial structure is clearly evident when inspecting samples along depth surfaces plotted in plan view in monthly intervals (e.g., Figure 3c). A monthly interval also corresponds to the Nyquist period associated with the time to complete each circuit, the minimum period resolved by half-monthly sampling [*Koopmans*, 1974]. Considering the above factors, 1 month was subjectively taken to be the shortest time scale on which horizontal gradients can be reliably resolved by the spatial survey.

In the near-surface layers, changes in temperature or salinity due to atmospheric forcing can occur across the survey pattern at time scales that are short relative to the time required for a glider to complete one survey. This results in time variability that is not necessarily described well by a second-order polynomial, as used in (1). An example of such a process is an "episodic cooling" event in which the mixed layer cools rapidly over a large area during 1–2 days (described at OSP by *Large et al.* [1986], *Large and Crawford* [1995], and *Dohan and Davis* [2011]). An example of rapid cooling in the mixed layer can be seen in observations of θ at $z = -10$ m in August 2009 (Figure 4). Figure 4a shows that SG144 sampled two abrupt decreases in temperature at $z = -10$ m in late August. When plotted in plan view, some spatial structure is evident (warmer temperatures to the southwest), but this is occluded by the rapid temperature change (Figure 4d).

The moored temperature sensor at $z = -10$ m, near the center of the Seaglider survey pattern (Figure 2a), also recorded two abrupt temperature decreases in late August 2009, though the timing differs from the Seaglider record, implying residual spatial differences. If it is assumed that the spatial and temporal variability are separable within the survey region—i.e., that temporal changes occur uniformly across the survey pattern, and that passing atmospheric variability leaves any horizontal structure unaltered—subtracting the moored record from the glider record would serve to isolate the spatial structure sampled by the Seagliders. Figure 4c shows the quantity $\theta_a = \theta - \theta_{moor}$, where θ_{moor} is the moored temperature record that has been low-pass filtered to remove superinertial variance and interpolated to glider sample times. Persistent spatial structure is much more clearly evident in θ_a than θ, in support of the assumption of space/time separability in this month (Figure 4e). The horizontal gradient can then be estimated by performing a regression fit to θ_a, rather than θ, where the regression equation is of a similar form to (1) but omits all t'_k terms (see best fit line in Figure 4c and gradient in Figure 4e). Application of this procedure to the estimation of surface temperature gradients after June 2009, when the NOAA OCS mooring was present, improved agreement between Seaglider-estimated gradients and those from gridded, satellite-based products (details provided in the SI), providing further support to the validity of the assumption of space/time separability. As a result, in an effort to reduce the effects of smearing in the boundary layer on the fortnightly Seaglider surveys, the above procedure—performing regression fits to glider data from which the moored time record has been subtracted—was used to estimate horizontal gradients of all scalar variables with the exception of $[O_2]$ in the upper 100 m for temporal intervals after June 2009.

The monthly intervals in which horizontal gradients and geostrophic velocity profiles (described below) are estimated averages over high-frequency and small-scale noise, due partially to internal waves, tides, and inertial oscillations. This noise contributes to residuals between the observations and the best fit line (e.g., Figures 3a and 4c). Confidence bounds on the horizontal gradient components (parameters B and C as described above) were calculated by assessing the sensitivity of the best fit coefficients to a random sampling of this noise. This is a variation on the procedure of bootstrap sampling of the regression residuals, one well-known method for assessing uncertainty on regression coefficients [*Wu*, 1986]. In each depth bin, after the best fit line was estimated, random noise was added to the fit at each sample, with variance and temporal
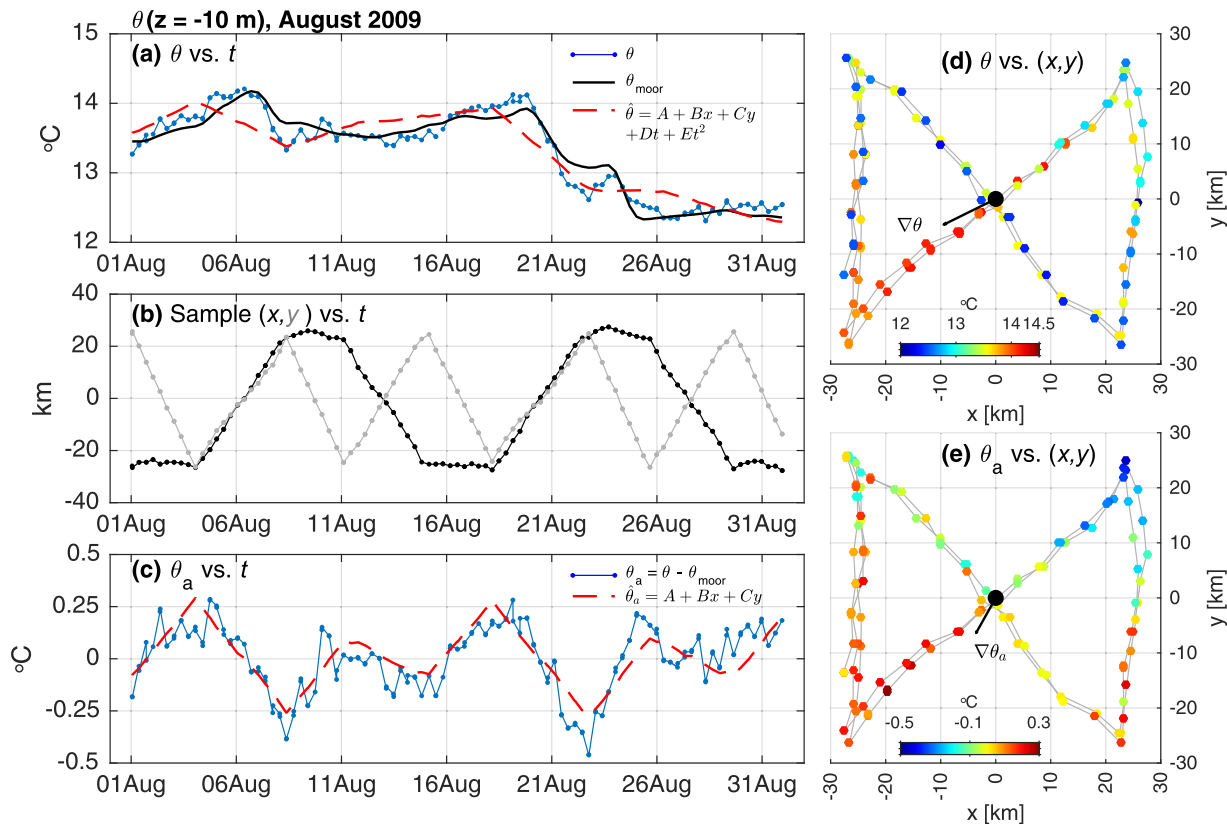
Figure 4. Example estimation of spatial gradient of potential temperature at 10 m depth $\theta(z=-10\,\text{m})$ in August 2009. (a) θ versus time t observed from Seaglider (blue curve), NOAA mooring (θ_{moor}, black curve, filtered to remove inertial oscillations), and regression fit to Seaglider observations of form (1) ($\hat{\theta}$, red dashed curve). (b) Seaglider sample eastward x (black) and northward y (gray) position versus t. (c) $\theta_a = \theta - \theta_{\text{moor}}$ versus t (blue) and regression fit using spatial terms only (red dashed curve). (d and e) θ and θ_a, respectively, in plan view with estimated horizontal gradient vectors plotted as in Figure 3c (scale: 10 km = 0.5°C per 50 km). Note different color scale range in Figure 4e versus Figure 4d.

autocorrelation of the noise prescribed to be similar to that of the residuals between observations and the original fit. Following the addition of noise, a second fit was performed to the noise-perturbed data from that iteration. This was repeated for 100 iterations, and 95% confidence bounds of B and C were estimated as two standard deviations of the noise-perturbed values of these coefficients over the 100 iterations.

2.2.2. Geostrophic Circulation

Estimated horizontal gradients of in situ density ρ estimated by the above procedure were used to compute vertical shear of eastward u_g and northward v_g components of geostrophic velocity in each monthly interval using the thermal wind equations:

$$\frac{\partial u_g}{\partial z} = \frac{g}{\rho f}\frac{\partial \rho}{\partial y}, \; \frac{\partial v_g}{\partial z} = -\frac{g}{\rho f}\frac{\partial \rho}{\partial x}, \tag{3}$$

where g is the gravitational acceleration, and $f = 1.1172 \times 10^{-4}\,\text{s}^{-1}$ is the Coriolis parameter at 50°N. Vertical integration of these yields monthly profiles of geostrophic velocity relative to 1000 m. For each component, absolute monthly geostrophic velocity was estimated by adding a constant to these profiles, whose value was equal to the difference between a monthly average of DAC estimated during each Seaglider cycle and the 0–1000 m average of the monthly relative velocity. The assumption that the monthly average DAC signal is purely geostrophic introduces error $\mathcal{O}(0.1)\,\text{cm s}^{-1}$ for typical values of monthly average Ekman transport at OSP [*Pelland*, 2015].

2.3. Additional Data Sets

This study uses several additional data sets in order to compare the results obtained from Seaglider surveys at OSP to climatological conditions, regional oceanography, or remote sensing. Climatological temperature, salinity, and oxygen concentrations were obtained from the World Ocean Atlas (WOA) 2013 climatology [*Boyer et al.*, 2013] (http://www.nodc.noaa.gov/OC5/woa13/). Estimates of sea surface height and

geostrophic circulation were obtained from the AVISO All-Satellite Absolute Dynamic Topography (ADT) product (http://aviso.altimetry.fr/index.php?id=1271). This product gives a daily estimate of sea-surface height on a 1/4° spatial grid. The effective spatial resolution of this data set is reduced in comparison to the grid resolution due to smoothing inherent in the mapping algorithm [*Chelton et al.*, 2011]. The ADT data set is computed as the sum of mapped satellite sea level anomaly and a mean dynamic topography as described in *SSALTO/DUACS* [2015] and *Rio et al.* [2013]. The All-Satellite version of this data set uses all available instruments in the altimetry satellite constellation at any one time to optimize horizontal resolution, with the trade-off that error statistics within the data set may not be uniform over the time period considered [*Chelton et al.*, 2011].

Data from the Argo autonomous float array (http://www.argo.ucsd.edu) interpolated to isopycnals were obtained from the Asia-Pacific Data-Research Center (APDRC; http://apdrc.soest.hawaii.edu/projects/argo/, accessed 21 May 2015), based on Argo profile data available at http://doi.org/10.17882/42182. Most Argo floats collect CTD profiles from 2000 dbar to the surface every 10 days, drifting at a typical parking depth of 1000 dbar between profiles; the target float density would be sufficient to give a nearest-neighbor separation of approximately 350 km [*Freeland*, 2013]. A total of 30,837 profiles were used from the APDRC product within 43°N–65°N, 180°W–120°W from 27 April 2001 and 7 May 2015.

Profile CTD data collected during 23 Line P occupations by the CCGS *Tully* from late summer 2007 (Cruise 2007-15) through winter 2015 (Cruise 2015-01) were obtained from the DFO Line P website (https://www.waterproperties.ca/linep/); these cruises overlap with the NOAA OCS moored time series. The *Tully* performs three cruises per year (winter, early summer, and late summer), during which at each station along Line P shown in Figure 1, a cast to at least 2000 dbar, or the bottom depth when shallower, is performed when weather allows using a SBE 911+ CTD (https://www.waterproperties.ca/linep/sampling.php). Other variables sampled on these casts, along with additional data collected at select Line P stations, are not discussed here. The data from these cruises are also compared to climatological properties on Line P as provided by Marie Robert (IOS-DFO). Climatologies were computed from data collected from Line P sampling 1956–1991 and are available for each calendar month (http://www.pac.dfo-mpo.gc.ca/science/oceans/data-donnees/line-p/data-eng.html).

Wind stress curl estimates were derived from the NCEP/NCAR Reanalysis 1 (R1) product [*Kalnay et al.*, 1996], provided by the NOAA Office of Oceanic and Atmospheric Research Earth System Research Laboratory Physical Sciences Division (http://www.esrl.noaa.gov/psd/data/gridded/data.ncep.reanalysis.html). The R1 product provides estimates of surface atmospheric variables, based on data assimilation of observations into a forecast model, at 6-hourly resolution on an approximately 2°×2° global grid.

3. Results

3.1. Upper-Ocean Structure

Seaglider surveys provide a persistent, high-resolution picture of the upper-ocean vertical structure at OSP. Figure 5a and Figure 6a, respectively, show daily-average Seaglider samples of θ and S as a function of z and t. The upper ocean at OSP is commonly delineated into a series of layers that are distinguished by their thermal and haline stratification as illustrated in these figures. The upper most of these layers is the surface *mixed layer* (ML), the maximum depth of which (MLD) is here defined as the depth at which daily-average potential density increases by an increment of 0.03 kg m^{-3} from its value at 10 m [*Cronin et al.*, 2015]. The ML at OSP has a strong annual cycle that reflects the variability in surface wind and net surface heat flux buoyancy forcing, with the deepest MLDs observed during February–March and shallowest during July–August [*Li et al.*, 2005]. During Seaglider surveys, the ML thickness varied from a minimum of 11 m on 17 July 2009 to a maximum of 128 m on 26 March 2009 (Figures 5a and 6a).

During the winter months (January–March), the ML extends vertically to nearly the top of the *halocline*, a layer of strong salinity stratification that is present throughout the subarctic North Pacific Ocean (Figure 6a) [*Dodimead et al.*, 1963; *Favorite et al.*, 1976]. The halocline is defined here as the layer between the $\sigma_\theta (\equiv \rho_\theta -1000)=26$ kg m^{-3} and $\sigma_\theta =26.8$ kg m^{-3} isopycnals, consistent with *Tabata* [1965]. The upper boundary had a minimum (maximum) depth of 93 m (138 m) on 6 August 2008 (26 March 2009), with a mean depth of 119 m. The lower boundary had a minimum (maximum) depth of 178 m (267 m) on 6 August 2008 (16 March 2009), and mean depth of 237 m. Within the halocline, temperature is nearly isothermal (Figure 5a).
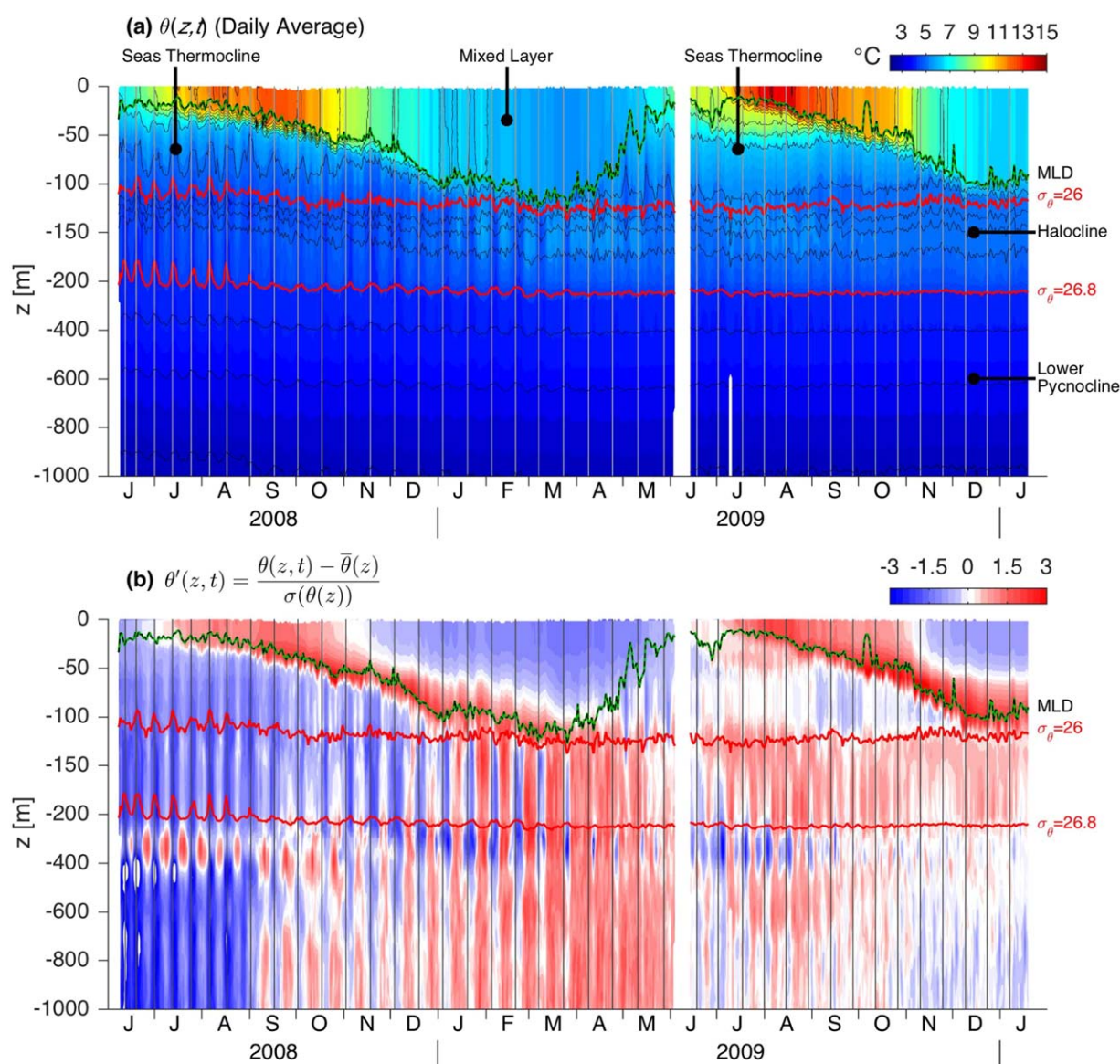
Figure 5. Daily average potential temperature θ versus z and t sampled by Seagliders during Ocean Station Papa (OSP) surveys. In both plots, note change of scale of z deeper than $z = -200$ m. In Figure 5a, background colors indicate θ, while black lines are potential density contours (interval 0.2 kg m^{-3}). Labels in Figure 5a indicate upper ocean layers at OSP. Red contours highlight potential density surfaces that form the upper and lower boundaries of the halocline, and the black-green dashed line indicates the mixed-layer depth (MLD). Vertical gray lines indicate times at which a Seaglider achieved the northwest target of the navigational pattern, beginning a new survey (Figure 2). (b) θ anomalies from the time-mean vertical profile, normalized by the depth-dependent standard deviation $\sigma(\theta(z))$. Here the mean vertical profile and standard deviation have been computed over the duration of the Seaglider surveys.

The strong density stratification in the halocline prevents its erosion due to turbulent entrainment forced by strong winter winds and surface buoyancy loss. Deeper than the halocline lies a layer of permanent thermal and haline stratification referred to here as the *lower pycnocline* [*Dodimead et al.*, 1963; *Tabata*, 1965]. This layer extends below the 1000 m depth range of Seaglider profiles.

In spring, downward surface buoyancy flux restratifies the water column and weakening surface winds allow a shoaling of the MLD. The ML warms as it shoals, and turbulent diffusion redistributes this heat downward from the ML—this results in a warm-season, thermally stratified layer known as the *seasonal thermocline* [*Dodimead et al.*, 1963; *Tabata and Giovando*, 1963]. Here the seasonal thermocline is defined to be the layer deeper than the ML and shallower than the halocline, within the months April–November (Figure 5a).

When viewed as a time series, approximately fortnightly periodicity is apparent in the temperature record at all depths greater than the MLD (Figure 5a). These periodic fluctuations are due to repetition of the survey
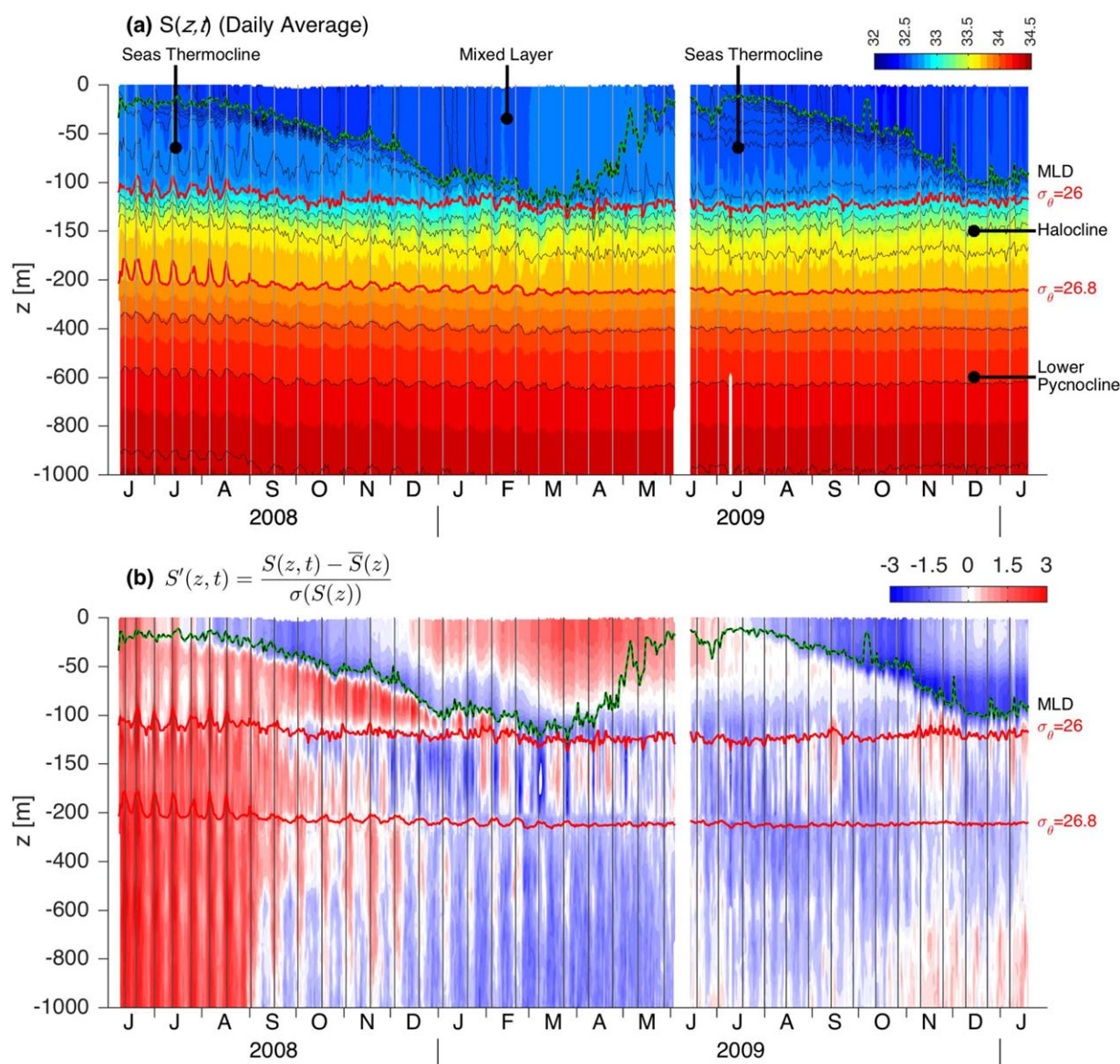
Figure 6. Daily average salinity S versus z and t sampled by Seagliders during Ocean Station Papa surveys, drawn as for θ in Figure 5.

circuit across spatial structure, as indicated by vertical gray lines plotted each time the vehicle achieved the NW target in Figure 5a. Similarly, periodic fluctuations in isopycnal depth are apparent, as well as an overall increase in the depth of isopycnals located deeper than the ML during the time series, and a weakening of stratification (vertical spreading of isopycnals) in the halocline (Figure 5a). Vertical displacement of the halocline during Seaglider surveys and the OCS moored time series is explored in more detail in section 4.

The pattern-periodic fluctuations in θ are easily seen when the temporal mean vertical temperature stratification is removed and the remaining anomalies normalized by the standard deviation of potential temperature at each depth (denoted $\theta'(z,t)$; Figure 5b). The mean stratification, and standard deviation of θ, are in this case computed over only the duration of the Seaglider surveys. At depths greater than 100 m, the vertically coherent time striations in the θ' record strongly suggest spatial variability across the survey track that is resolved by the Seaglider surveys. Shallower than 100 m, the striations are less visually distinguishable from the large seasonal anomalies generated by the heating, cooling, and deepening of the surface boundary layer. These features of the θ' record suggest that spatial changes dominate the variance in θ at depths >100 m, while temporal changes dominate the variance shallower than this depth. Low-frequency time

variability is evident deeper than 100 m in the form of a net warming of these waters over the course of the time series. In the halocline and lower pycnocline, peak temperatures were observed between January–May 2009, coincident with the greatest downward displacement of isopycnals in these layers.

The salinity time series exhibited weaker seasonality in the ML and seasonal thermocline relative to the amplitude of vertical variations than temperature (Figure 6b). Within the ML, S was at a minimum in late summer and early fall and a maximum when the ML was deepest in late winter. Vertically coherent periodicity is also apparent in $S'(z,t)$, defined similarly to $\theta'(z,t)$ as above, at depths >100 m (Figure 6b). Low-frequency salinity variability on depth surfaces was in the opposite time sense as temperature variability, consistent with downward displacement of isopycnals in the presence of a positive vertical temperature gradient and negative vertical salinity gradient (Figures 5 and 6).

3.2. Water Mass Properties

A temperature-salinity-depth diagram constructed from all Seaglider profiles in the halocline demonstrates that water mass properties within this zone varied throughout the survey time series (Figure 7). Two dominant θ-S modes were observed: a cool mode, with halocline temperatures between 4°C and 4.5°C, and a warm mode with temperatures >5°C. These two water mass modes in the halocline are evident in a histogram of θ along the $\sigma_\theta = 26.5$ kg m^{-3} isopycnal (Figure 8a), which lies within the halocline at a mean depth during these surveys of 151 m. Sorting profiles into histograms in seasonal intervals indicates that the cool mode was most often observed in the first seasonal interval (June–September 2008, Figure 8b) and the warm mode was most often observed in the final interval (October 2009 to January 2010, Figure 8b), with intermediate water masses observed within the interior of the time series. Some temperatures that exceeded the mean within the warm mode were observed on $\sigma_\theta = 26.5$ kg m^{-3} in early 2009 (Figure 8b).

Variability in θ along isopycnals in the halocline was investigated for any associated variability in [O$_2$]. On $\sigma_\theta = 26.5$ kg m^{-3}, [O$_2$] was 15–20 μmol kg^{-1} higher in the warm mode than cool mode (Figure 9c), with a correlation coefficient r between the two variables of 0.84. The statistical significance of this coefficient was tested using a Student's t test, where the sample test statistic $t_{samp} = r\sqrt{(N^*-2)/(1-r^2)}$ is compared to t_{crit}, the 95% bound of a Student's t distribution with degrees of freedom N^*-2. Here N^* is the effective sample size of the
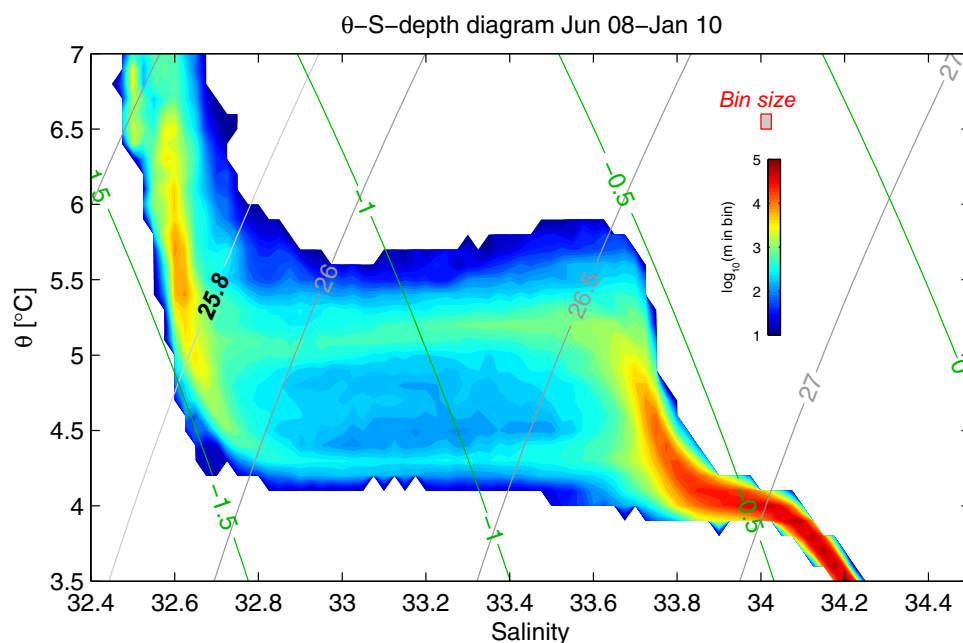

Figure 7. Potential temperature (θ)-salinity (S)-depth diagram composed from Seaglider profiles during surveys at Ocean Station Papa. Diagram is constructed by sorting all Seaglider samples into bins in θ-S space, with bin size indicated by shaded square at upper right of diagram. Color contours indicate the sum of the vertical extent of all samples within each bin, in logarithmic scale. This diagram is equivalent to a θ-S-volume diagram if it is assumed that each profile corresponds to an equal horizontal spatial area [*Pelland et al.*, 2013]. Gray lines indicate density contours; $\sigma_\theta = 25.8$ kg m^{-3} (bold label) is the greatest density of the mixed layer observed during the time series. Green lines indicate contours of constant spice [*Flament*, 2002].
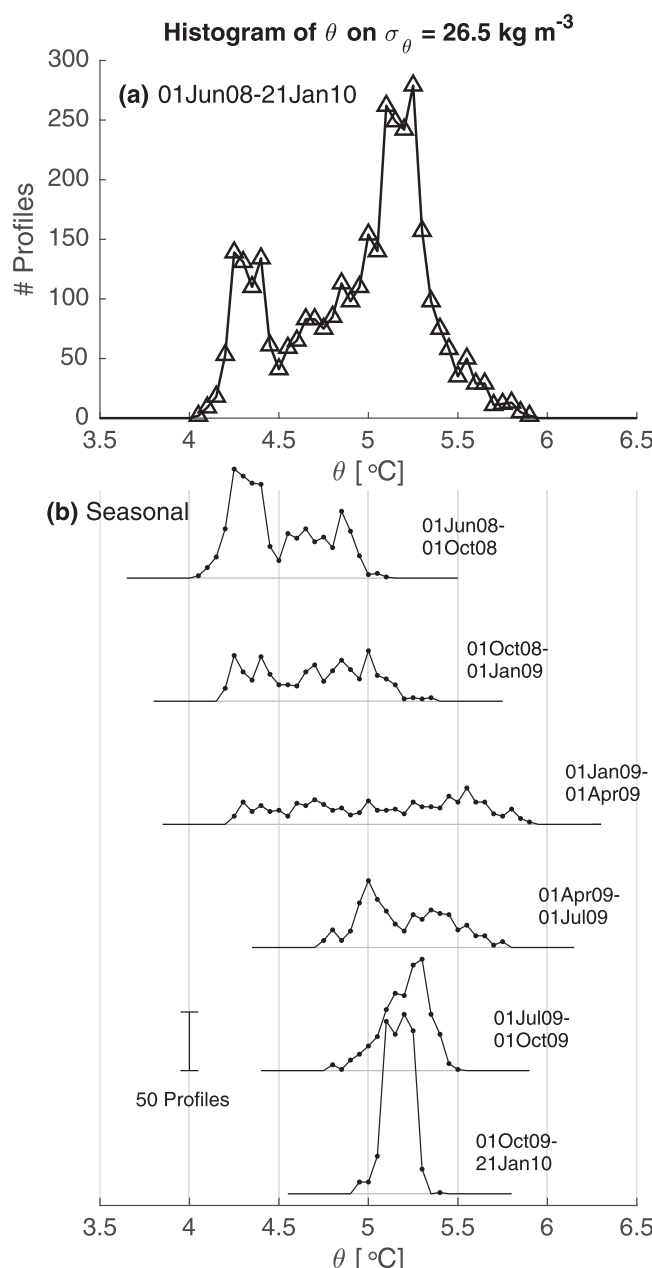
Histogram of θ on σ_θ = 26.5 kg m^{-3}

Figure 8. Histrogram of potential temperature θ along the σ_θ = 26.5 kg m^{-3} isopycnal, which lies within the halocline layer at OSP. (a) Histogram constructed from all Seaglider profiles during the array time series; (b) histograms constructed in seasonal intervals. The first and last intervals in Figure 8b are extended to include observations made in June 2008 and January 2010, respectively.

paired [O$_2$] and θ time series, taking into account any autocorrelation [Bretherton et al., 1999]. The effective number of independent samples on σ_θ=26.5 kg m^{-3} was determined to be 14 using methods described in Bretherton et al. [1999, equation (30)]. Using this sample size, the correlation coefficient between [O$_2$] and θ on σ_θ=26.5 kg m^{-3} is significantly different from zero (t_{samp}=5.45 > t_{crit}=2.18), confirming the elevated [O$_2$] values within the warm mode on this isopycnal. Correlations between [O$_2$] and θ were not significantly different from zero on either σ_θ=26 kg m^{-3} (r=−0.67, N^*=6, t_{samp}=1.82 < t_{crit}=2.78; Figure 9a) or σ_θ=26.2 kg m^{-3} (r=0.06, N^*=12, t_{samp}=0.77 < t_{crit}=2.23; Figure 9b).

3.3. Estimated Horizontal Gradients

The horizontal θ gradient vector at OSP $\nabla\theta$ is shown at selected depths in each month in Figure 10. Each horizontal gradient vector is drawn as in Figures 3c, 4d, and 4e—such that a vector pointing straight upward indicates increasing temperature to the north—and with its origin at the center of the depth bin and time interval to which the estimate corresponds. Gradients whose uncertainty ellipse (section 2.2.1) does not include zero are shown in black, while all others are shown in gray. Root-mean-square (RMS) values of the uncertainty in each of the four layers defined previously are drawn at right. Uncertainty on individual vectors is shown separately in the SI (Figure S5).

The results indicate that $\nabla\theta$ was strongest in the seasonal thermocline and halocline during the first half of the Seaglider time series (Figure 10). Its magnitude $|\nabla\theta|$ reached 0.25–0.5°C per 50 km (navigation pattern width). Magnitude was sometimes stronger than this in the upper seasonal thermocline. In the ML, $\nabla\theta$ was to the south and east in late 2008, and to the south and west in 2009 (Figure 10), though many estimates were not significantly different from zero in the latter time period. Within the halocline, $|\nabla\theta|$ weakened considerably after April 2009, and was strongest in the upper seasonal thermocline following this month. Horizontal potential temperature gradient observed in the seasonal thermocline and halocline until late 2009 was considerably stronger than the climatological southeastward $\nabla\theta$ estimated at OSP in the WOA 2013 decadal 1/4° 2005–2012 climatology, and was oriented predominantly eastward. The characteristic uncertainty ellipses indicate that horizontal gradients of θ are well resolved in the halocline and lower pycnocline. Examination of individual uncertainty ellipses indicates that the largest uncertainties are within the upper seasonal thermocline (SI).
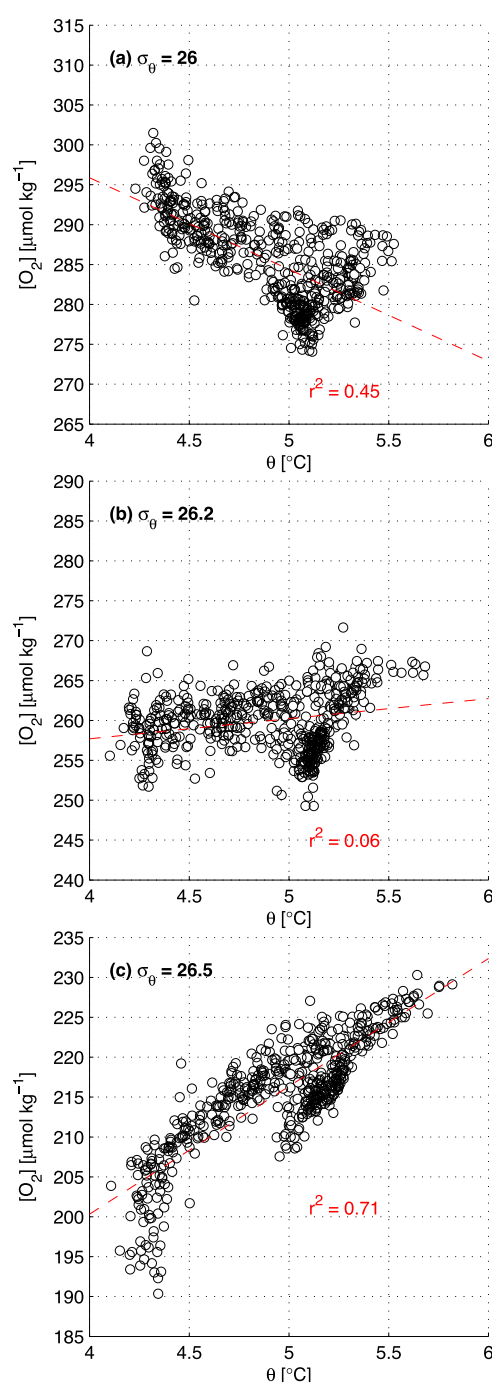
Figure 9. Dissolved oxygen concentration $[O_2]$ versus potential temperature θ on three isopycnals within the halocline at during Seaglider surveys at Ocean Station Papa: (a) $\sigma_\theta = 26$ kg m^{-3}, (b) $\sigma_\theta = 26.2$ kg m^{-3}, and (c) $\sigma_\theta = 26.5$ kg m^{-3}. In each plot, the red dashed curve is a linear trend line fit to $[O_2]$ versus θ (r^2 value listed in red text). The oxygen concentrations are significantly positively correlated with θ in Figure 9c.

Like $\nabla\theta$, the horizontal salinity gradient ∇S was of greatest magnitude in the halocline (Figure 11). In contrast to $\nabla\theta$, ∇S uncertainties were largest in this layer rather than in the ML and seasonal thermocline (uncertainty on individual vectors shown in Figure S6). Lower pycnocline ∇S is well resolved, similar to $\nabla\theta$. In early 2008, ∇S was nearly opposite in direction to $\nabla\theta$ in the seasonal thermocline and deeper, suggestive of downward vertical displacement of these layers in waters to the east. After this period, there is not a clear correspondence between the two gradients. Furthermore, $|\nabla S|$ did not weaken in the halocline after April 2009 to the same extent as $|\nabla\theta|$ (Figure 11). Also unlike $|\nabla\theta|$, $|\nabla S|$ was much weaker in the ML and upper seasonal thermocline relative to its strength in the halocline. The horizontal gradient of salinity at OSP in the WOA 2013 climatology has a maximum strength of 0.0142 per 50 km at 130 m depth, increasing along 287°T (Figure 11). Monthly ∇S estimated during the Seaglider surveys was an order of magnitude larger in strength (RMS magnitude of 0.1375 per 50 km at 130 m depth) than the climatological gradients and was oriented in the opposite direction for extended periods in the halocline (January–March 2009 in Figure 11).

3.4. Geostrophic Circulation

Estimated geostrophic velocities from Seaglider surveys (black vectors in Figure 12) were roughly unidirectional in the top 1000 m and weakly vertically sheared; the strongest currents were 5–10 cm s^{-1} in the top 200 m and <5 cm s^{-1} at greater depths. Flow was moderate and predominantly northward during 2008 and early 2009, before rotating counterclockwise to westward and weakening from March to May 2009, coinciding with the transition between strong, eastward $\nabla\theta$ and relatively weak gradients thereafter. Depth-average signals were near zero from November 2009 onward. The monthly profiles of geostrophic flow estimated from glider estimates of $\nabla\rho$ and DAC are in good qualitative agreement with monthly averages from the depth-mounted ADCP instruments (Figure 12). The ADCP also observed rotation of flow in March–May 2009 and weakening near the end of 2009, along with the presence of the strongest flow in the top 200 m. The glider-derived near-surface velocities agree with the monthly average surface geostrophic velocity time series calculated from AVISO ADT (Figure 12).

Also shown in Figure 12 are square vector correlation coefficients ρ_v^2, defined as in *Crosby et al.* [1993], between geostrophic velocity time series estimated by Seagliders and other platforms. These coefficients are presented to quantify the degree of correlation between vector time series derived from different platforms and to test whether these correlations are larger than that expected due to finite sampling of two independent and uncorrelated vector time series. The variable ρ_v^2 has possible values between 0 (two time
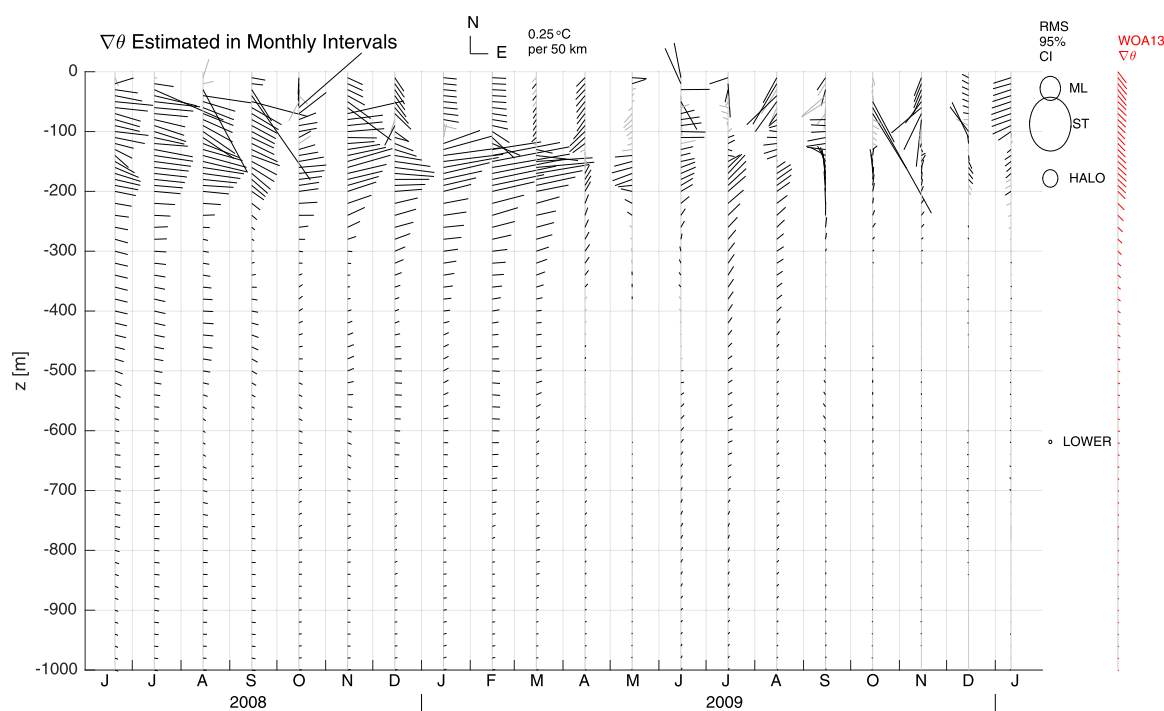
Figure 10. Vertical profiles of the horizontal gradient vector of potential temperature $\nabla\theta$ in monthly intervals estimated from Seaglider surveys at Ocean Station Papa (OSP). Gradient vectors are plotted as in Figures 3 and 4, with their origin at the depth level and center of the monthly interval in which they are estimated. For clarity, vectors are plotted every 10 m in the upper 200 m and every 20 m from 200 to 1000 m depth. North and east scale vectors are shown at top—a vector pointing straight upward indicates increasing temperature to the north. Ellipses at right indicate root-mean-square (RMS) 95% uncertainty bounds on horizontal gradients in four vertical layers as defined in Figures 5 and 6: surface mixed layer (ML), seasonal thermocline (ST), halocline (HALO), and lower pycnocline (LOWER). Uncertainty bounds described in section 2.2.1; black vectors indicate those whose uncertainty ellipse does not include zero. Profile of red vectors at far right indicates the $\nabla\theta$ estimated at OSP from the World Ocean Atlas 2013 (WOA13) 1/4° optimal interpolation decadal climatology for the period 2005–2012.
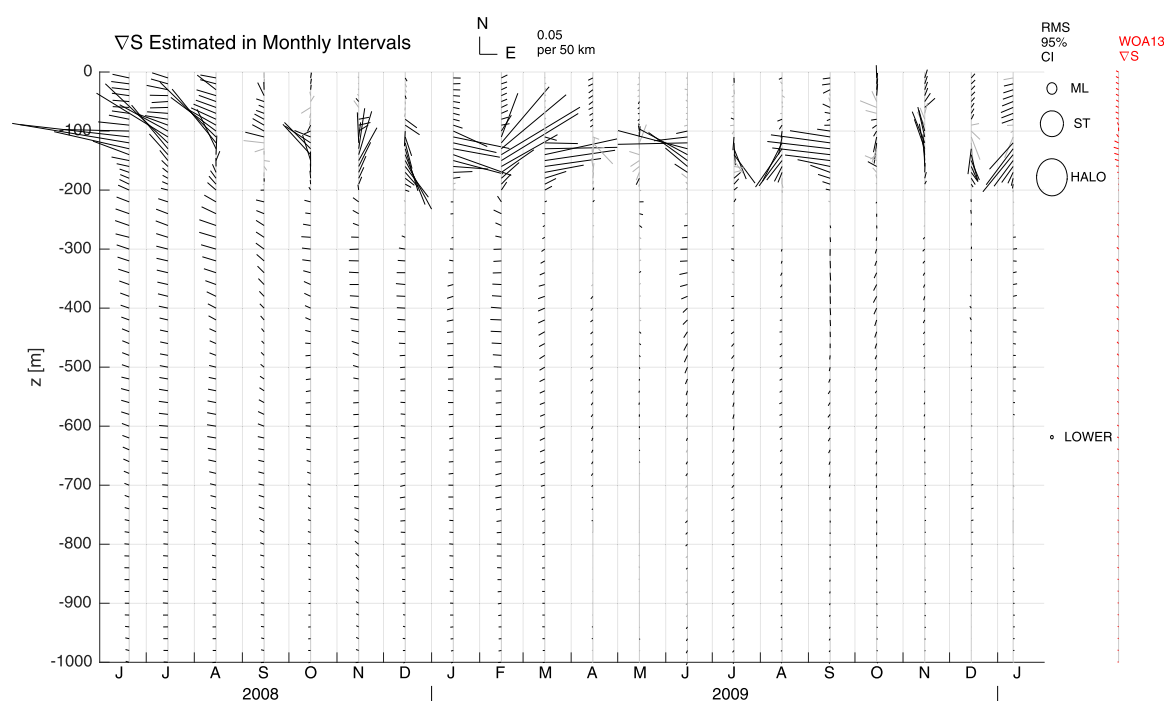

Figure 11. Vertical profiles of the horizontal gradient of salinity ∇S in monthly intervals estimated from Seaglider surveys at Ocean Station Papa, plotted as for θ in Figure 10.
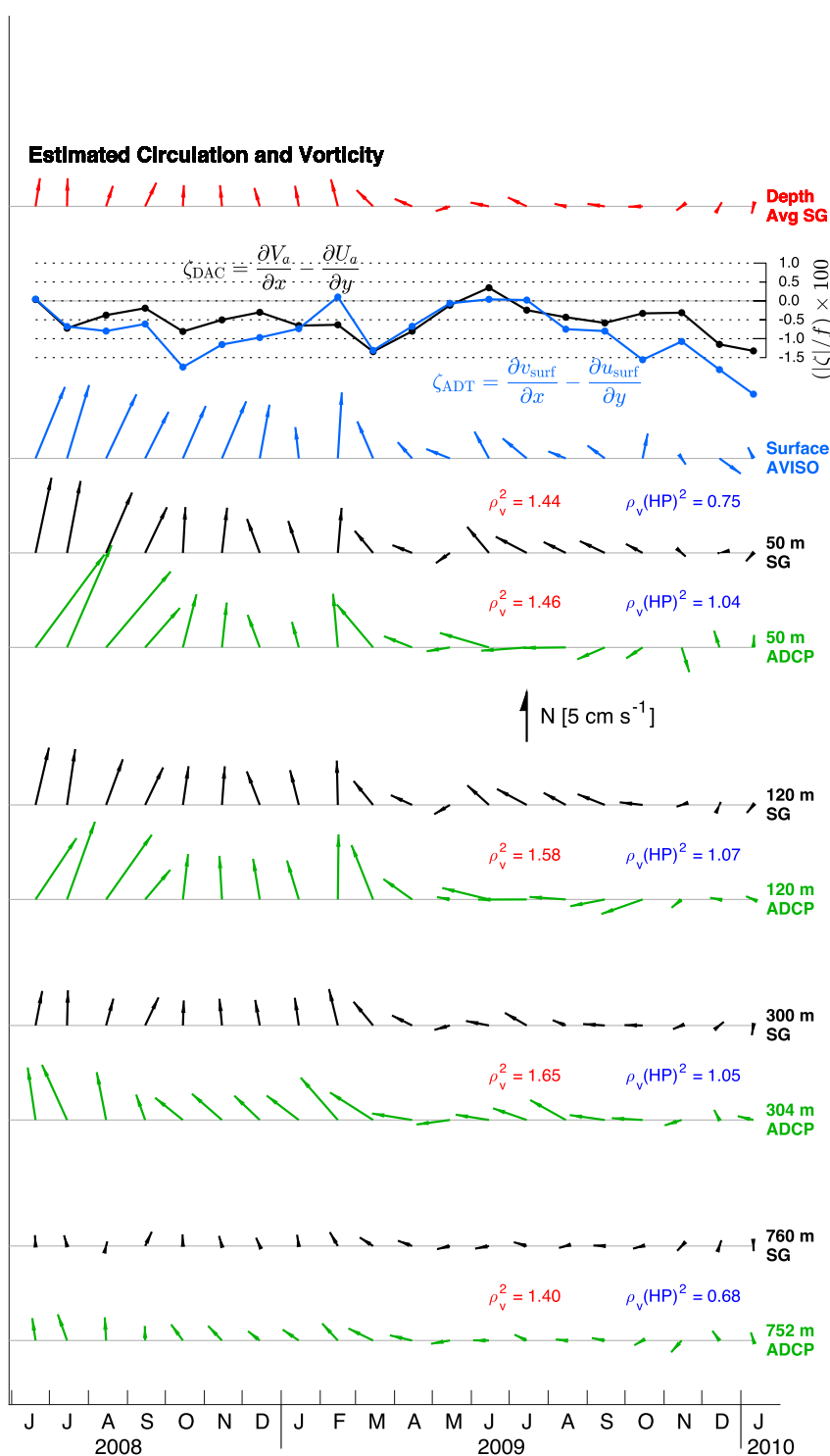
Figure 12. Horizontal circulation and vorticity during the Seaglider time series, estimated monthly. Top plot shows 0–1000 m Seaglider depth-averaged current (red), second plot from top shows estimated vertical vorticity of depth-averaged currents (ζ_{DAC}, black curve), and of surface currents from AVISO Absolute Dynamic Topography (ADT) all-satellite gridded product (ζ_{ADT}, blue curve). Third plot shows ADT surface velocity (blue arrows). The remaining plots show monthly mean Seaglider-derived (SG) absolute geostrophic velocity at four depths (50, 120, 300, and 760 m, black arrows) and monthly average ADCP velocity in the closest depth bin (green arrows). These depths were chosen to provide an accurate representation of the typical geostrophic velocity profile and to ensure that at least one depth was chosen within the upper and lower range of each of the two ADCP instruments. Text indicates the square vector correlation coefficient ρ_v^2 [*Crosby et al.*, 1993] between glider and ADCP/ADT velocities at each depth; each ρ_v^2 value is the observed correlation between the two vector time series shown immediately above and below that value.

series are independent) and 2 (perfectly correlated), where perfectly correlated vector time series are defined as those that are linearly dependent on one another—that is, one time series could be converted to the other by applying a uniform scaling factor and/or rotation angle. In this way, the ρ_v^2 variable quantifies whether two vector time series exhibit similar month-to-month changes in magnitude and direction, independent of the absolute amplitude of each time series. For a sample size of 20, $\rho_v^2 > 0.458$ indicates a square correlation coefficient significantly different than zero (details provided in the SI). The ρ_v^2 value between Seaglider geostrophic velocity and ADCP monthly average velocity at each depth level, and between 50 m Seaglider and ADT-derived surface velocity, everywhere exceeds this critical value (Figure 12). The results are similar between ADT-derived surface velocity and 10 m Seaglider geostrophic velocity (not shown; $\rho_v^2 = 1.47$).

These correlations are likely influenced by the low-frequency changes in circulation from modestly northward to weakly westward captured by both time series, which reduces the effective sample size. Hence, anomalies from this background circulation were estimated by subtracting a low-pass filtered vector time series obtained using a triangular-weight filter with 3 month half-window width. Although vector correlations between the anomalies (denoted by $\rho_v(\text{HP})^2$) were lower, all were still significant at 95% confidence (Figure 12).

Absolute geostrophic velocities estimated from the Seaglider surveys are dependent on both estimates of horizontal gradients and the monthly average DAC (section 2.2.2). Figure 13 shows the vertical geostrophic current difference estimated from the Seaglider surveys, which depends only on the gradient of density, over 250–800 m depth compared to the vertical current difference measured by the ADCP over the same interval. Vertical current difference is estimated here by a linear least squares fit to the monthly vertical profile. Both instruments showed the strongest current difference oriented poleward during the first three months of the Seaglider time series and in February 2009. The current difference backed and weakened in March–May 2009, as its orientation was aligned with the depth-averaged flow throughout the Seaglider surveys (Figure 12). The square vector correlation between the two platforms was $\rho_v^2 = 1.54$ for the monthly average current difference values and $\rho_v(\text{HP})^2 = 1.20$ for the high-passed filtered values. Both of these are significant at 95% confidence (Figure 13).

The observed circulation gives a Rossby number ($Ro \equiv U/fL$) [*McWilliams*, 2006] of 0.01, indicating highly linear flow that is approximated well by the geostrophic balance. Here $U = 0.05$ m s^{-1} and $L = 50$ km are, respectively, velocity and spatial scales corresponding to the phenomena observed during Seaglider surveys. As will be shown in section 4.4, mesoscale circulation patterns were of comparable scale to the survey pattern. An alternate definition of the Rossby number is formed using the ratio of the vertical vorticity of the flow $\zeta = \frac{\partial v}{\partial x} - \frac{\partial u}{\partial y}$ to f, $Ro_\zeta \equiv |\zeta|/f$ [e.g., *Holton*, 1992, section 4.4.3]. The depth-average current vorticity
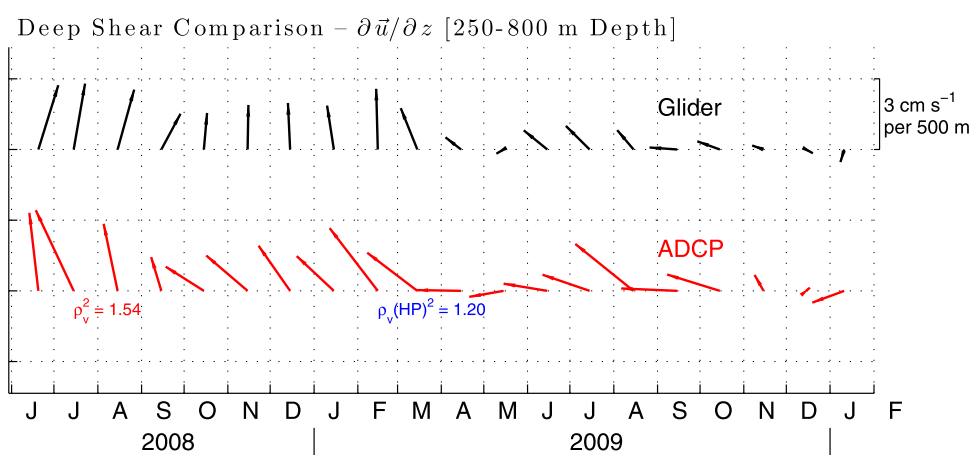

Figure 13. Comparison of vertical shear vectors in monthly intervals estimated from Seaglider sampling (black) and moored ADCP (red). Shear is computed over the depth range 250–800 m, which corresponds to the majority of the depth range of the lower instrument in the depth-mounted ADCP mooring, and is a depth range where the flow is expected to be geostrophic. Scale shown at upper right. The strength and direction of the vertical shear is similar to the depth-average current (DAC) signals of Figure 12. The square vector correlation coefficient for unfiltered (ρ_v^2) and high-pass filtered ($\rho_v(\text{HP})^2$) shear vectors between the two time series is also shown.
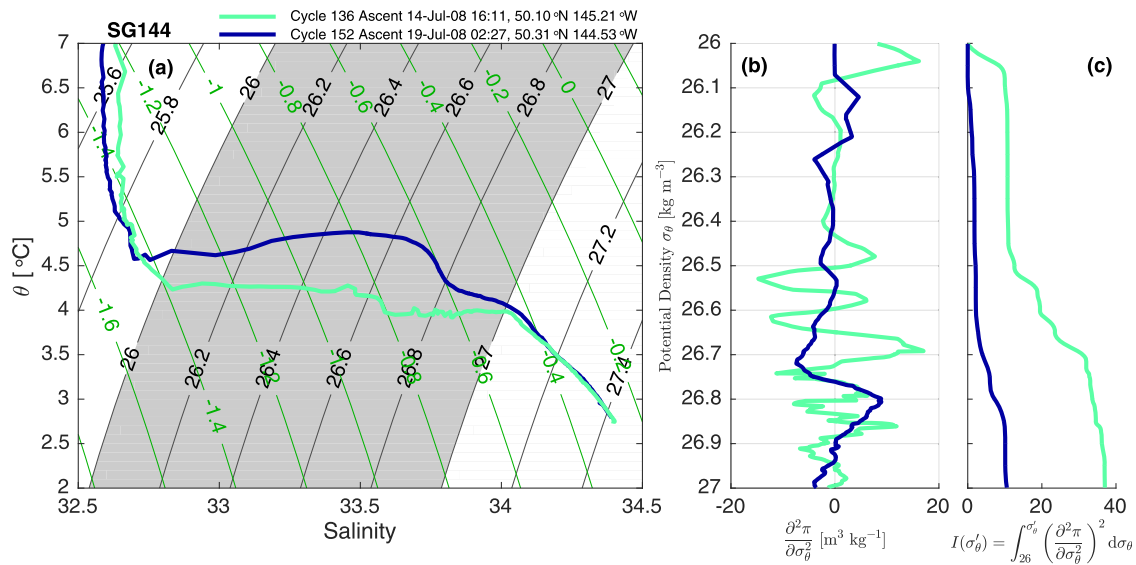
Figure 14. Two example profiles from Seaglider (SG) 144's June–August 2008 deployment, one of which (green profile) shows evidence of density-compensating θ variations characteristic of horizontal interleaving. (a) The potential temperature θ-salinity S characteristics of the two profiles. Black contours indicate potential density σ_θ surfaces and dark green contours indicate spice surfaces as defined by *Flament* [2002]. (b) The curvature of spice π with respect to σ_θ within the range $26 \leq \sigma_\theta \leq 27$ kg m^{-3} for the two profiles; this density range is also highlighted by gray shading in Figure 14a. (c) The quantity $I(\sigma_\theta')$ as described in the text; i.e., the integral with respect to density of the square of spice curvature, taken from $\sigma_\theta = 26$ kg m^{-3} to a density σ_θ'.

ζ_{DAC} was estimated in each monthly interval using least squares fits to each component of DAC as a function of x and y. The estimated ζ_{DAC} was predominantly anticyclonic and varied in strength over the range 0–1.5% of f, also giving $Ro_\zeta \approx 0.01$ (Figure 12). The time record of surface vertical vorticity estimated from the AVISO ADT product in monthly intervals was similar to that of ζ_{DAC}, consistent with the weakly vertically sheared flow (Figure 12).

3.5. Vertical Fine Structure

In addition to gradients in water mass properties across the survey track, selected profiles contained evidence of density-compensating variations in θ and S in the halocline and lower pycnocline, suggestive of horizontal interleaving observed at thermohaline fronts. At such fronts, where two water masses with similar density profiles, but different θ-S characteristics meet horizontally, thin horizontal intrusions of one water mass into the other may form due to mesoscale stirring or double-diffusive instability [*Ruddick and Richards*, 2003]. When such lateral intrusions occur, the θ-S curves of profiles collected vertically through an intrusion exhibit abrupt jumps in slope (vertical fine structure) near the density surfaces that form the upper and lower boundaries of the intrusion, as the profile moves vertically through layers that have different θ-S relationships. Temperature-salinity characteristics of two example profiles, one of which displays evidence of such fine structure while the other does not, are shown in Figure 14. These profiles were collected in July 2008 and are representative of the range of fine structure features observed across a single survey. Within the halocline and lower pycnocline, the warmer of the two profiles appears smooth in θ-S, while the other exhibits small variations in temperature along isopycnals deeper than $\sigma_\theta = 26.4$ kg m^{-3}.

The net incidence of fine structure was quantified in each Seaglider profile, for the purposes of investigating its relative prevalence through time during the period spanned by Seaglider surveys. This was done using a method developed by *Shcherbina et al.* [2009], who quantified the presence of thermohaline intrusions at the North Pacific Subtropical frontal zone using "spice" π, a variable that identifies thermohaline anomalies along isopycnals. For two water parcels with the same potential density, but differing combinations of temperature and salinity, the warmer parcel is said to have higher spice. We adopt the widely used definition of *Flament* [2002], specifying curves of constant spice that have equal-magnitude slope and opposite sense to isopycnals in the θ-S plane (green contours in Figure 14). Spice defined in this way has been used previously in investigations of fine structure at frontal regions [e.g., *Shcherbina et al.*, 2009; *Pelland et al.*, 2013].
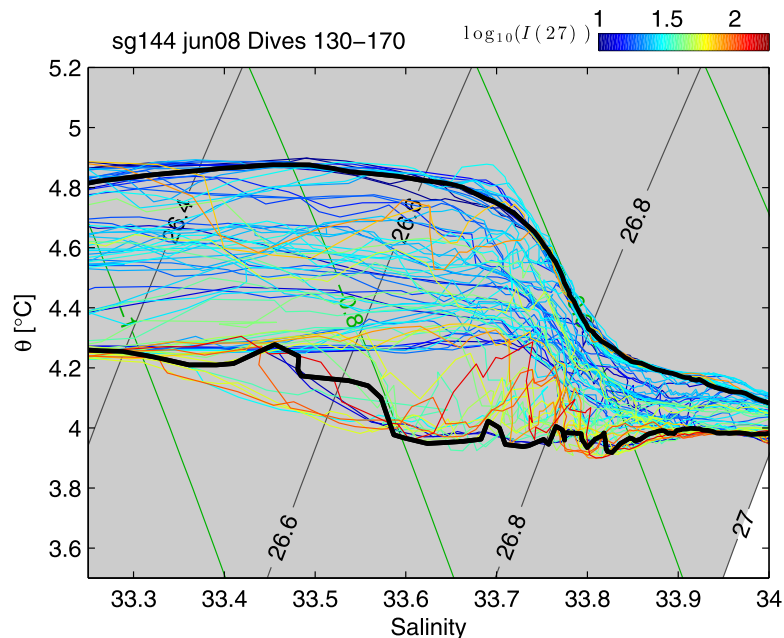
Figure 15. Detail of potential temperature θ-salinity S structure in profiles collected during Seaglider (SG) 144 cycles 130–170, 12 July to 24 July 2008. Plot is centered on the lower portion of the halocline. Profiles are plotted with color corresponding to the logarithm of their integrated square spice curvature [I(27)], with color scale at upper right. Example profiles from Figure 14 are plotted as solid black lines.

Specifically, the net incidence of fine structure in a profile was quantified using the curvature of π with respect to potential density σ_θ, $\partial^2\pi/\partial\sigma_\theta^2$. The spice defined by *Flament* [2002] has the same units as density, therefore its derivative with respect to density is unitless, and its curvature has units of specific volume (m³ kg^{-1}). The quantity $\partial^2\pi/\partial\sigma_\theta^2$ is a useful indicator of intrusion-like fine structure, because the abrupt jumps in π versus σ_θ at the upper and lower interfaces of intrusion features result in large magnitudes of the second derivative there. Profiles of spice curvature were computed here by linearly interpolating π to isopycnals, estimating the curvature with respect to density using a second-order accurate finite-difference approximation, and then filtering the results with a triangular-weight filter with half-width of 0.05 kg m^{-3} to remove noise with diapycnal scales smaller than that of the observed features. It is assumed in this procedure that any fine structure is of sufficiently low vertical:horizontal aspect ratio that its observed structure is unaffected by slantwise Seaglider profiling. Figure 14b shows spice curvature for the two example profiles. The cooler profile in Figure 14 (green curves) has more numerous and stronger-magnitude $\partial^2\pi/\partial\sigma_\theta^2$ maxima and minima than the warmer profile (blue curves).

To quantify the net incidence within a profile, the square of the curvature is computed, and integrated across the density range in which fine structure was typically observed. Figure 14c shows the quantity

$$I(\sigma_\theta') = \int_{26}^{\sigma_\theta'} \left(\frac{\partial^2\pi}{\partial\sigma_\theta^2}\right)^2 d\sigma_\theta; \; \sigma_\theta' > 26, \tag{4}$$

which is zero for a profile that has constant π within the bounds of integration, is otherwise positive, and increases for profiles with either large-magnitude or numerous incidences of thermohaline fine structure. Note that this quantity is also functionally equivalent to the RMS spice curvature within profiles used by *Shcherbina et al.* [2009] to assess the relative prevalence of fine structure across a frontal survey. Here the integral is taken from the upper boundary of the halocline at $\sigma_\theta = 26$ kg m^{-3} to $\sigma_\theta = 27$ kg m^{-3} [I(27)]; these density surfaces were determined to be the isopycnal surfaces between which most observed fine structure was confined. The quantity I(27) is nearly 4 times larger for the cool example profile than the warm one in Figure 14c.

Figure 15 shows θ-S detail near the base of the halocline for a series of profiles collected 12–24 July 2008, including the two example profiles shown in Figure 14. Here the profiles are colored by the logarithm of
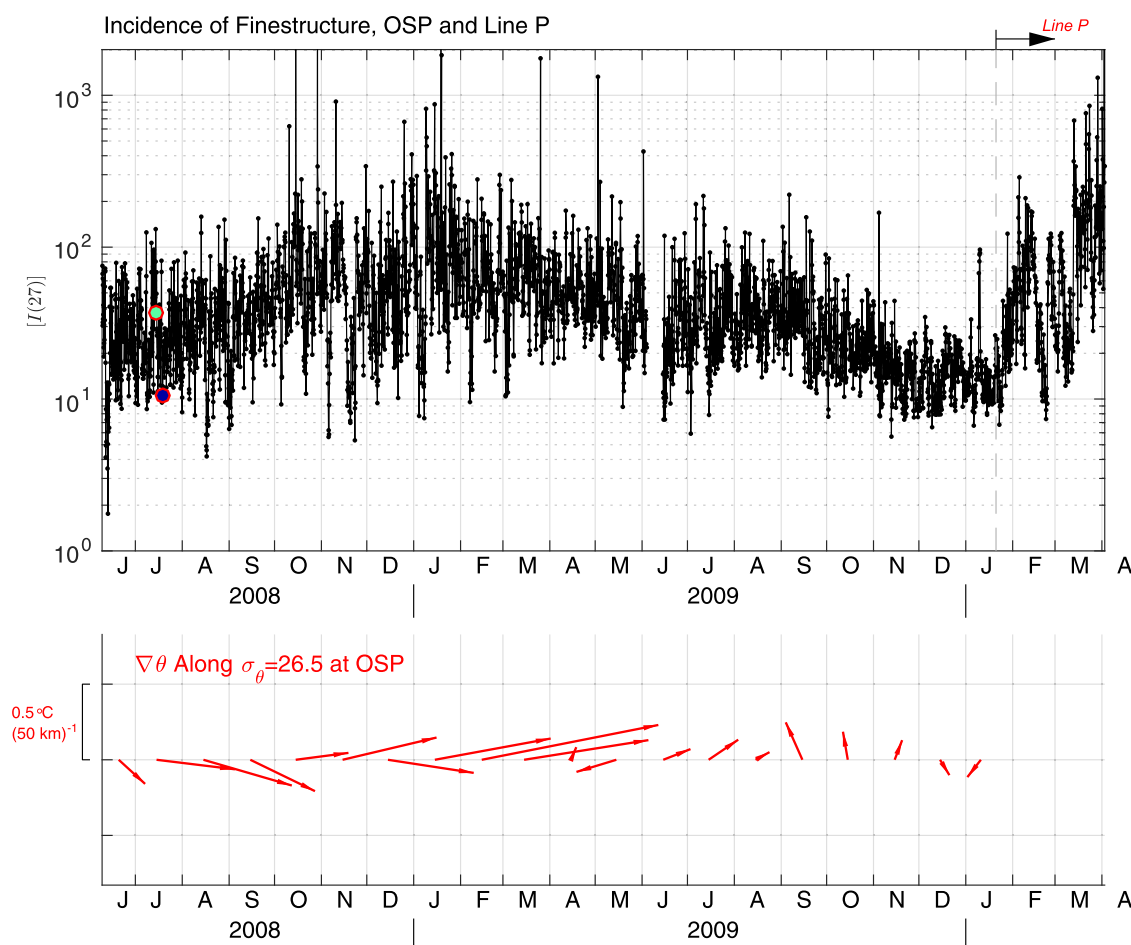
Figure 16. (top) Time series of integrated square spice curvature I(27), indicative of the presence of vertical θ-S fine structure within individual Seaglider profiles. Green and blue dots in the top plot correspond to the two example profiles shown in Figure 14. The time period shown corresponds to the full extent of Seaglider surveys at Ocean Station Papa (OSP) in addition to Seaglider 144's transit inshore along Line P (Figure 1). (bottom) The time series of the horizontal gradient of potential temperature on σ_θ=26.5 kg m^{-3} (scale at left; vector pointing straight up indicates increasing temperature to the north).

their I(27) score. In general, less sinuous profiles with fewer incidences of fine structure have lower I(27) scores. Profiles with the largest I(27) were consistently closer to the cool θ-S mode for this time period. The two example profiles shown in Figure 14, indicated by black lines, bound the upper and lower range of θ observed along isopycnals during this period.

The time series of fine structure incidence as quantified by I(27) is consistent with the evolution of water mass properties within the halocline. Peak θ-S fine structure was observed during October 2008 to March 2009 (Figure 16). These are months in which temperature along σ_θ=26.5 kg m^{-3} showed the greatest variability (Figure 8), consistent with water mass contrasts across the navigational track pattern. This is also in agreement with estimates of ∇θ along σ_θ=26.5 kg m^{-3}, which were computed using the same multivariable linear regression methods as described in section 2.2.1 (Figure 16). Fine structure decreased after March 2009, coincident with backing and weakening of the geostrophic circulation, and a reduction in strength of the isopycnal temperature gradient in the halocline. The weakest I(27) was observed in November 2009 to January 2010, during a period when warm mode temperatures were consistently observed along σ_θ=26.5 kg m^{-3} (Figure 8) and horizontal gradients of temperature along this isopycnal were weak (Figure 16).

Fine structure increased again during SG144's transit inshore along Line P, and levels similar to those in winter 2008–2009 at OSP were observed in February and late March 2010. This occurred as the vehicle encountered a series of thermohaline fronts (not shown) associated with the transition between cool, fresh offshore subarctic water and warm, saline inshore equatorial-influenced water along Line P [*Klymak et al.*,

2015]. Horizontal variations of $I(27)$ at OSP were examined within each month; fine structure appeared spatially patchy with no clear horizontal dependence in most months, with the exception of January 2010 when weak fine structure was clearly localized in the SW corner of the navigational pattern (not shown).

4. Discussion

4.1. Survey Performance

The utility of Seaglider surveys for sampling mesoscale spatial gradients in the bowtie pattern fundamentally depends on whether the mesoscale field evolves sufficiently slowly at OSP that it can be captured by surveys that repeat every 14.5 days. The consistency of geostrophic velocity signals obtained independently between the ADCP, AVISO surface dynamic topography, and Seaglider-surface mooring array confirms that this is the case, with sufficiently low error such that a qualitatively accurate profile of geostrophic velocity can be constructed at monthly intervals. The significant correlation between monthly average Seaglider and ADCP vertical shear in the lower ADCP instrument zone (250–800 m depth), where the flow is assumed to be entirely geostrophic, indicates that Seagliders can adequately resolve horizontal spatial gradients in density in this depth range. This is also consistent with the small confidence bounds relative to the size of the estimated gradients of θ and S there.

Correlation in absolute velocities, even after high-pass filtering to remove the seasonal-scale flow, indicates that monthly mean DAC signals from Seagliders are also capturing monthly anomalies in geostrophic circulation. The negative relative vorticity estimated from DAC is also consistent with the surface vorticity estimated from AVISO, and with the observed properties of near-inertial internal waves from the ADCP time series by *Alford et al.* [2012]. These authors noted observations of greater-than-expected energy in internal wave motions at frequencies below *f*. In an ocean with a resting background state, the inertial frequency *f* forms the lower frequency bound for propagating internal waves. A background flow with anticyclonic vorticity ($\zeta < 0$), as was the case for much of the Seaglider survey period, effectively lowers this bound and allows waves at frequencies below *f* [*Kunze*, 1985; *Alford et al.*, 2016].

As noted in section 2.2.1, estimation of horizontal gradients is made more difficult by rapid time variability within the ML and the thermally stratified layer beneath it, which together compose the oceanic boundary layer that is directly influenced by atmospheric forcing. Previous studies near OSP found significant variation of near-surface horizontal gradients at the 1–2 day time scale of passing storms [*Large et al.*, 1986; *Torruella*, 1995]. Even in the case that horizontal gradients are left unchanged by a passing storm, the smearing of events like these onto fortnightly surveys can result in ambiguity over whether observed changes are due to spatial or temporal variability [*Rudnick and Cole*, 2011]. Correspondingly, despite using the moored time series to attempt to isolate spatial structure sampled by Seagliders after June 2009, resolution of horizontal gradients in Seaglider surveys at OSP was poorest in the ML and upper seasonal thermocline for $\nabla\theta$. For ∇S, uncertainties were largest in the halocline, likely due to small-scale horizontal structure and internal wave noise, though gradients were still robustly resolved there in many months.

Rapid time variability in the upper-ocean boundary layer likely presents the greatest challenge to estimation of horizontal gradients in future deployments. Though quantitative analysis of the optimum configuration of gliders and moorings at this and other time series sites is beyond the scope of the present study, multiple autonomous vehicles in combination with a surface mooring is likely a more tractable approach for in situ estimation of gradients in the surface boundary layer. Glider sampling could also be altered to increase vehicle buoyancy thrust and profiling speed, and/or decrease the maximum depth to which gliders profile, at the cost of decreased vehicle endurance. Seaglider surveys intended to resolve submesoscale upperocean horizontal gradients at a similar time series site in the North Atlantic Ocean have used multiple vehicles, more rapid profiling, and a smaller survey pattern than described here [*Damerell et al.*, 2016; *Thompson et al.*, 2016].

4.2. Conditions at OSP

Seaglider surveys at OSP observed weak and highly linear geostrophic circulation, which is consistent with the characterization of the southern GOA as a low-kinetic energy region. The pattern of currents observed during the Seaglider surveys is contrary to the expectation of moderate northeastward climatological flow at OSP. This was consistent with horizontal water mass gradients, density gradients, and suggestions of
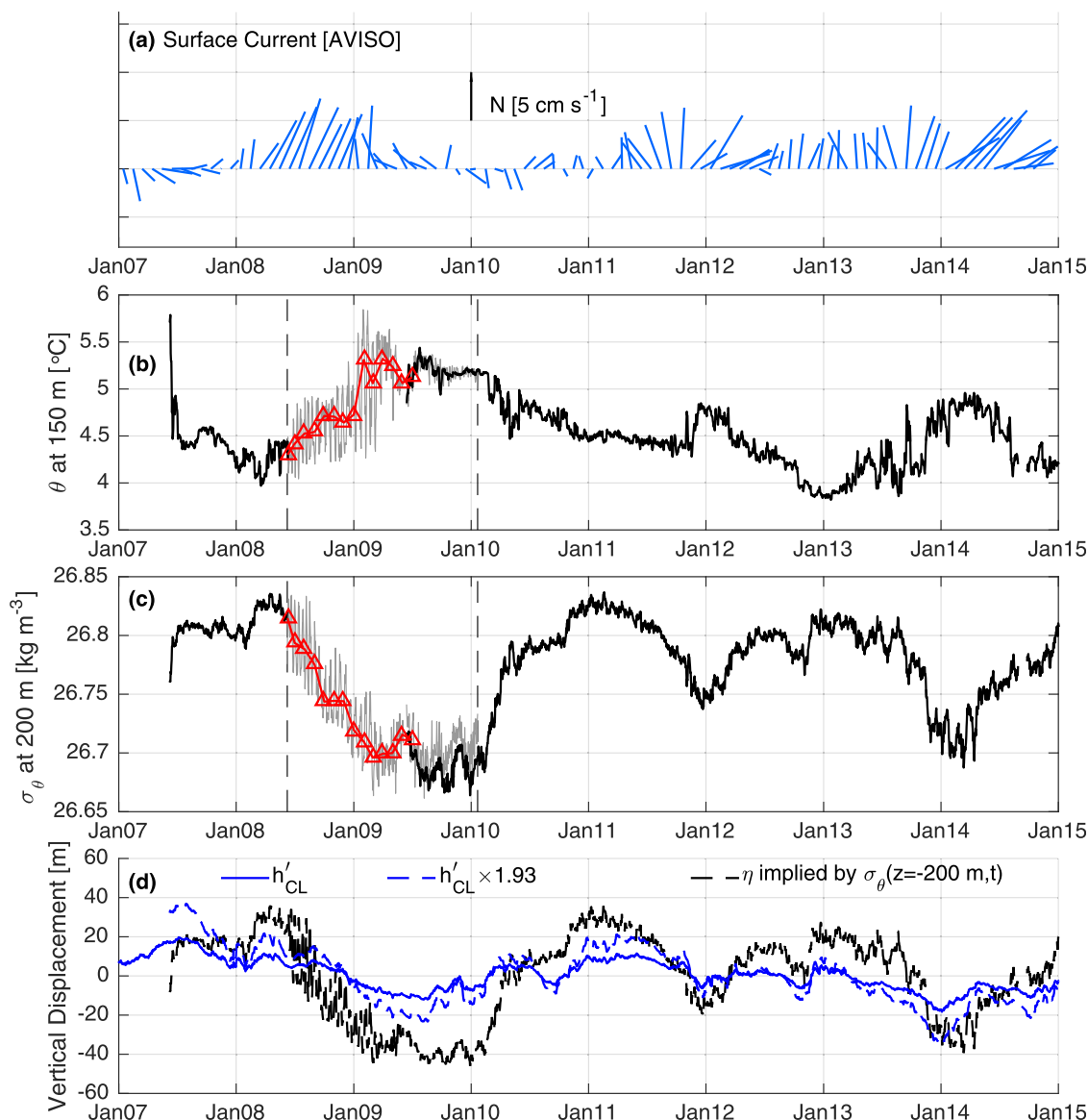
Figure 17. Records of (a) surface circulation, (b) potential temperature θ at 150 m, (c) potential density σ_θ at 200 m, and (d) vertical displacement at 200 m during the Ocean Station Papa (OSP) mooring time series. Vertical dashed lines in Figures 17b and 17c indicate the time bounds of the Seaglider surveys at OSP. In (b) and (c), black curves indicate the mooring record, while gray curves indicate Seaglider samples. Red curves indicate monthly estimates of θ or σ_θ at the mooring location during mooring absence. In Figure 17d, black dashed curve indicates vertical displacement η implied by Figure 17c as defined in section 4.4, blue curve indicates wind stress curl-forced displacement predicted by the model (5), denoted h'_{CL} [*Cummins and Lagerloef*, 2002], and blue dashed curve indicates h'_{CL} scaled to provide best fit to η. Curves are offset such that the time-mean of each is zero during 8 June 2007 to 31 December 2014.

thermohaline frontal structure within the halocline and lower pycnocline that are not usually described there, although they are common in the subarctic-subtropical transitional domain to the south [*Roden*, 1977a; *Lynn*, 1986; *Roden*, 1991]. Examination of the moored record and AVISO surface circulation from the time of OCS mooring deployment from 2007 onward indicates that downward displacement of isopycnals and weakened geostrophic velocity was anomalous in comparison to the remainder of the 2007–2014 period covered by the mooring time series (Figures 17a and 17c). Weak southward circulation was also observed at the start of the mooring time series in 2007 (Figure 17a).

The downward vertical displacement of isopycnals in the halocline and lower pycnocline observed during Seaglider surveys also appears unusual in comparison to the longer OSP observational record. Potential density at 200 m reached a minimum value near 26.7, suggestive of large downward displacement, during the latter half of the Seaglider time series (Figure 17c). A second prolonged period of similar character was evident in early 2014, while two smaller-magnitude downward displacement events were observed in

winter 2011–2012 and in late 2012. From the record of density anomalies in the upper ocean over the 1956–2005 Weathership and IOS sampling period published by *Whitney et al.* [2007, Figure 2], it appears there was only one other occasion where the 26.7 isopycnal—normally located at 150–175 m depth—reached 200 m, during the passage of a coastally generated mesoscale anticyclonic eddy in 1974.

Previous studies have also quantified the vertical displacement of isopycnals in the halocline using an objective measure of the core depth of stratification h, whose definition is based on winter vertical density profiles [*Freeland et al.*, 1997]. For comparison, this quantity was computed from daily-average Seaglider observations of σ_θ during January–April 2009 using the least squares method described in *Freeland et al.* [1997]. The mean estimated h in this period was 134.5 m, among the deepest values observed at OSP and approximately 20 m deeper than expected based on previous observations of this quantity and its long-term trend as presented in *Freeland and Cummins* [2005, Figure 10].

4.3. Water Mass Origins

Changes in circulation and isopycnal displacement were also coincident with an abrupt transition in water mass properties during Seaglider surveys. Aside from a brief peak observed in June 2007, θ at 150 m reached its maximum value over the moored time series during the latter portion of Seaglider surveys at OSP (Figure 17b). The thermal stratification at 150 m is too weak for this maximum to be accounted for solely by vertical displacement of isopycnals, implying a change along isopycnals, as observed by Seagliders. Although the warm mode θ, S, and associated downward isopycnal displacement, is suggestive of North American coastal water sometimes transported to OSP by anticyclonic eddies [*Crawford et al.*, 2007; *Whitney et al.*, 2007; *Lyman and Johnson*, 2015], warm mode water also had elevated oxygen concentrations along isopcynals in the lower halocline. This is evidence against the interpretation of the warm mode as coastal water, since coastally generated anticyclones in the GOA contain oxygen-poor water sourced from the diluted signature of equatorial water found along the North American continental slope [*Aydin et al.*, 1998; *Castro et al.*, 2001; *Crawford et al.*, 2007; *Thomson and Krassovski*, 2010]. Previously sampled coastally generated eddies at or near OSP had temperatures ∼6°C or greater and oxygen concentrations 150–175 μmol kg^{-1} or less on $\sigma_\theta = 26.5$ kg m^{-3} [*Crawford et al.*, 2007; *Whitney et al.*, 2007].

The warm mode properties found at OSP are similar to what *Aydin et al.* [1998] term the Western Subpolar Water (WSW), which lies on the northern edge of the subtropical-subarctic frontal zone, intermediate in temperature, salinity, and oxygen characteristics between the two gyres [*Aydin et al.*, 1998, 2004]. On $\sigma_\theta = 26.5$ kg m^{-3}, WSW has [O$_2$] ∼225 μmol kg^{-1} and θ of 4.5–5.5°C, depending on the longitude and degree of mixing between the WSW and surrounding subarctic water as it travels eastward along the NPC. *Aydin et al.* [2004] attribute the increased [O$_2$] in WSW relative to its surroundings to more recent ventilation and modification of these waters in the Kuroshio-Oyashio confluence region. The oxygen concentrations and temperatures observed in the cool mode at OSP appear intermediate between WSW and those of Alaska Gyre water [*Aydin et al.*, 2004], which has halocline temperatures near 4°C and [O$_2$] ∼175 μmol kg^{-1} along $\sigma_\theta = 26.5$ kg m^{-3}.

Figure 18 shows spatial locations of Argo autonomous float profiles that sampled water in the NPC and GOA with temperatures along $\sigma_\theta = 26.5$ kg m^{-3} similar to the cool and warm modes at OSP for the period 2001–2015. In agreement with *Aydin et al.* [1998, 2004], profiles with warm mode temperatures to the west of OSP were sampled along the northern margin of the NPC. Profiles with warm mode temperatures in the northeastern and western GOA reflect the advection of WSW by the prevailing currents and the influence of remnant equatorial water along the North American coast [*Thomson and Krassovski*, 2010]. By contrast, Argo float profiles with cool mode temperature characteristics are generally found within the GOA gyre.

Observations of dissolved oxygen from the Argo array are not as widespread, preventing a similar analysis for [O$_2$]. However, areas with dissolved oxygen concentrations on $\sigma_\theta = 26.5$ kg m^{-3} consistent with the warm and cool modes in the WOA 2013 annual climatology are also shown by shaded contours in Figure 18. Areas with climatological θ and [O$_2$] properties consistent with the cool (warm) mode can therefore be inferred by where the blue (red) shaded area overlaps with blue dots (red triangles) in this figure. These results confirm that the cool mode properties are typically found within the central GOA, either to the north or northwest of OSP, while the warm mode properties are found from the southwest through southeast of OSP, within 1–2° latitude.

The Argo samples in Figure 18 show a region of spatial overlap in areas where warm mode and cool mode temperatures were observed during 2001–2015; OSP lies within this region. Seaglider 144 also observed
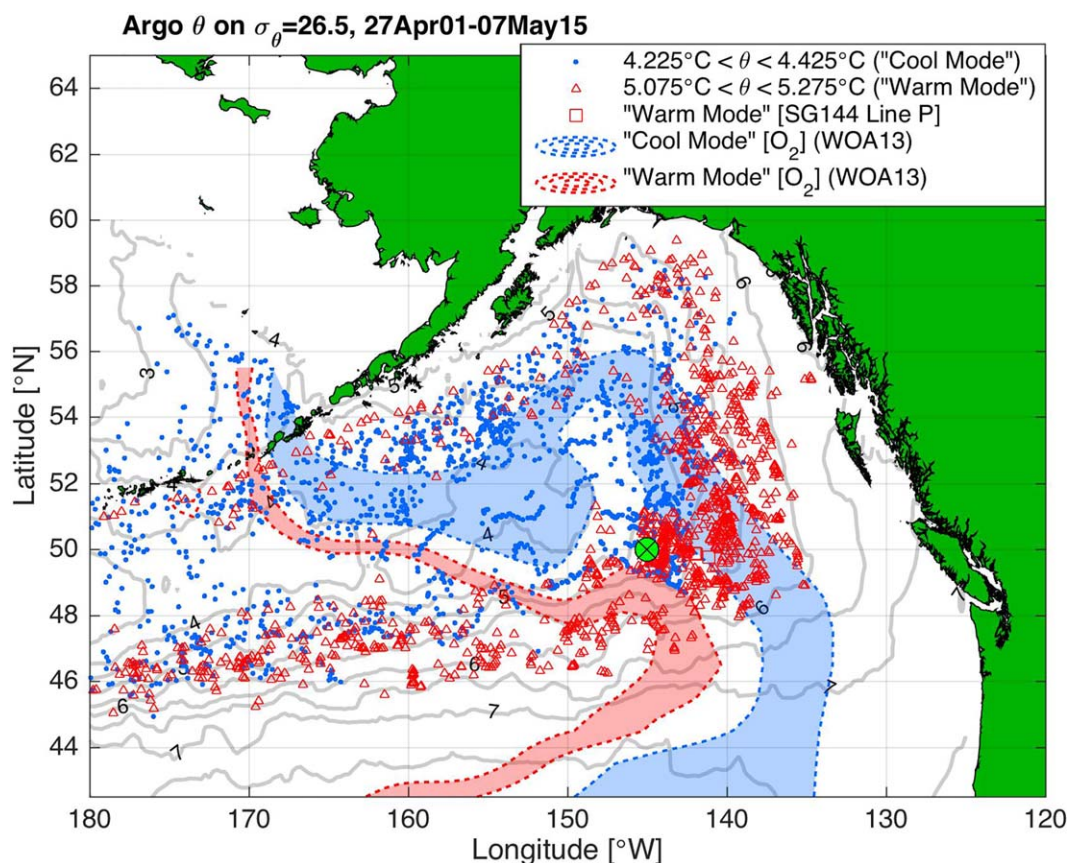
Figure 18. Observations of water mass properties similar to warm and cool modes observed during Seaglider surveys at Ocean Station Papa. Gray contours show bin-averaged values of θ on $\sigma_\theta = 26.5$ kg m^{-3} from the Argo array during 2001–2015 ($n = 30{,}837$ total profiles) with bin center spacing of 0.25° and 2°×2° bin size. Red triangles (blue circles) show individual Argo profiles with θ on this isopycnal similar to "warm" ("cool") modes. Red squares indicate profiles with temperature and oxygen concentrations similar to the warm mode in Seaglider 144's Line P crossing (cool mode properties were not observed there). Red (blue) shading corresponds to regions with oxygen concentrations on this isopycnal similar to the warm (cool) mode in the World Ocean Atlas 2013 (WOA13) annual climatology. Green cross-circle indicates the Ocean Station Papa site.

temperatures and oxygen concentrations consistent with the warm mode in three profiles between 141°W and 142°W on its crossing of Line P (Figure 18). The spatial scatter of profiles in which properties similar to either mode were observed is consistent with the description of the NPC as meandering and eddy rich, resulting in stirring of these two water masses. The results of *Whitney et al.* [2007] suggest that the properties of either water mass mode are not particularly anomalous relative to the full range of conditions in the OSP record (*cf.* their Figure 4).

4.4. Possible Explanations for Observed Phenomena

One notable feature of the phenomena observed during Seaglider surveys is the vertical displacement of isopycnals within the halocline. Previous studies have found that vertical displacement in this layer, as quantified by the variable h defined in section 4.2, exhibits interannual variability of $\pm\sim25$ m and a shoaling trend of 56 m per century [*Freeland et al.*, 1997; *Cummins and Lagerloef*, 2002; *Freeland and Cummins*, 2005]. *Cummins and Lagerloef* [2002] found that the trend and much of the interannual variability in h were well explained by a first-order Markov model forced by Ekman upwelling:

$$\frac{dh'}{dt} = w_e - \lambda h' \tag{5}$$

with $\lambda^{-1} = 1.5$ year a damping time scale, $w_e = (\nabla \times \vec{\tau})(\rho f)^{-1}$, $\vec{\tau}$ is the surface wind stress vector, and here h' is the vertical displacement anomaly (positive upward) rather than its absolute value. This model conceptualizes low-frequency vertical displacement as a local response to wind forcing (omitting remote forcing due

to baroclinic Rossby waves) that is damped by small-scale local processes parameterized by the $\lambda h'$ term. Figure 17d shows an estimate of wind-forced displacement predicted by the model (5), denoted h'_{CL}, computed using unfiltered R1 wind stress curl [*Cummins and Lagerloef*, 2002].

This displacement predicted by the above model is compared to an estimate of vertical displacement implied by observed density changes at 200 m during the OCS mooring time series, denoted η (Figure 17d). Since the observational definition of h is based strictly on winter vertical profiles of density (section 4.2), the variable η was used instead to provide a continuous estimate of vertical displacement throughout the moored time series. This variable was constructed under the reasoning that if the shape of the vertical density profile remains unchanged in the lower halocline, then density changes at 200 m imply vertical displacements of this profile. The quantity η is defined as follows:

$$\eta(t) = -\left[d_{\sigma_\theta}(t) - \overline{d_{\sigma_\theta}}\right]. \tag{6}$$

For a given value of $\sigma_\theta(t)$ observed at 200 m during the moored time series, $d_{\sigma_\theta}(t)$ is the interpolated depth of that value in the mean vertical profile of σ_θ during Seaglider surveys, $\overline{\sigma_\theta}(z)_{SG}$. The variable $\overline{d_{\sigma_\theta}}$ is the mean value of $d_{\sigma_\theta}(t)$ during the mooring time series. The estimate η is not sensitive to the choice of temporal interval over which $\overline{\sigma_\theta}(z)_{SG}$ is computed (results not shown).

The h'_{CL} predicted from the model (5) correlates with the estimated η ($r = 0.67$), but is of insufficient magnitude to explain the large downward displacement in 2009–2010. A least squares fit to η as a function of h'_{CL} yields an optimum gain in h'_{CL} of 1.93. Even after application of this gain, the estimated magnitude of h'_{CL} in 2009–2010 is only half that of η (Figure 17d). Although this exercise does not rule out wind stress curl as a contributor to the observed displacement during the Seaglider surveys, it suggests that displacement was dominated by a process other than local wind stress curl forcing.

Local wind stress curl-driven displacement cannot in any case directly explain changes in properties along isopycnals. Previous investigators have found explanations for such variability at OSP in gyre-scale circulation changes. In an analysis of hydrographic data in the GOA from 1955 to 1958, *Tully et al.* [1960] found similar deep warm anomalies at OSP, and noted that these were coherent with increased temperatures on isopycnals between OSP and Vancouver Island from January 1957 to August 1958. *Tully et al.* [1960] attributed this to an increase in the poleward component of advection in the NPC across the subarctic front, south of which lies relatively warm and saline water along isopycnals [*Yuan and Talley*, 1996; *Johnson et al.*, 2012; *Taguchi et al.*, 2015, Figure 18].

Figure 19b shows Line P θ anomalies on $\sigma_\theta = 26.5$ kg m^{-3}, where the anomalies are computed relative to the Line P monthly climatology 1956–1991. Contrary to the phenomenon observed by *Tully et al.* [1960], warm mode waters at OSP during Seaglider surveys were not coherent with warm anomalies elsewhere along Line P (Figure 19b)—i.e., during 2009, when warm mode waters were consistently observed at OSP, predominantly negative or neutral temperature anomalies were observed inshore of station P23 during three Line P occupations. Some warm anomalies were observed at P14 and P10 in summer 2009, though these were not widespread. Interestingly, following the conclusion of Seaglider surveys, coherent warm anomalies across much of Line P were observed in 2010–2011, coincident with increased poleward flow in the NPC (Figures 19a and 19b) and consistent with the concept of advection of warm and saline water across the subarctic front as posited by *Tully et al.* [1960]. Though further exploration of these anomalies is beyond the scope of this study, large-scale changes in subsurface water mass structure in the GOA and neighboring California Current System influence the pelagic ecosystem through alterations in nutrient availability and preferred habitat [*Tully et al.*, 1960; *Freeland et al.*, 2003; *Sydeman et al.*, 2011], and their potential generation due to shifts in NPC orientation warrants continued observation.

In light of the downward isopycnal displacement and negative relative vorticity, a plausible alternate explanation for the phenomenon observed during the Seaglider time series is the presence at OSP of an anticyclonic mesoscale eddy or meander that originated within the WSW region, possibly as a result of baroclinic instability in the interior of the NPC [*Gill*, 1974; *Robinson and McWilliams*, 1974; *Chelton et al.*, 2011]. Such a possibility was suggested by *Thomson et al.* [1990] based on drifter observations of eddying flow in the interior GOA. Three month averages of AVISO ADT, along with observations from Argo, Seagliders, and the CCGS *Tully*, provide several pieces of evidence that support this scenario (Figure 20). Observations of increasingly warm and saline water in the halocline in the eastern portion of the Seaglider survey pattern
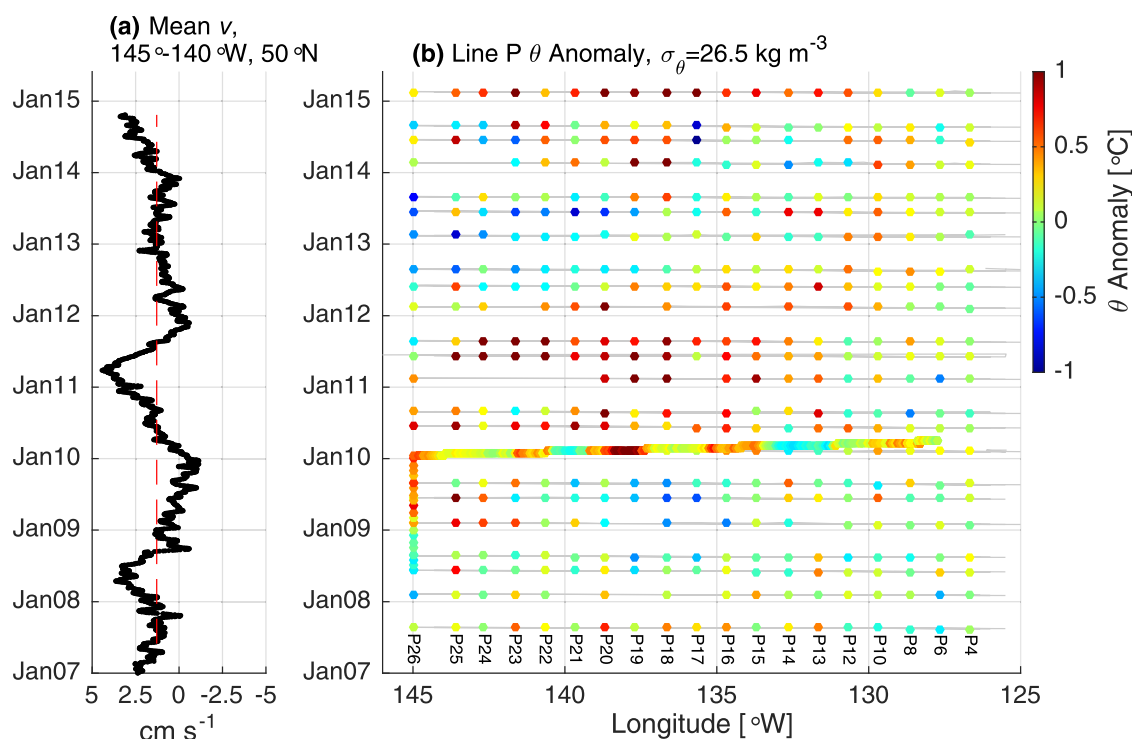
Figure 19. (a) Time series of zonal-mean surface poleward flow at 50°N, 140°W–145°W, derived from AVISO ADT product. Dashed red line indicates time-mean, June 2007 onward. (b) Line P (Figure 1) potential temperature θ anomaly on $\sigma_\theta = 26.5$ kg m^{-3}. Anomalies are computed from monthly Line P climatologies constructed from data 1956–1991 at each station (labels at bottom). For Seaglider 144's transit along Line P (January–April 2010), mean θ versus longitude determined from the Line P time series was linearly interpolated to each Seaglider observation.

were coincident with a weak sea surface height undulation in the NPC appearing near OSP during spring (April–June) and summer (July–September) 2008 (Figures 20a and 20b). This feature grew in amplitude in winter (January–March) through summer 2009, appearing at this time as an anticyclonic meander with its crest to the northwest of OSP near 51°N, 147°W (Figures 20d–20f). In autumn (October–December) 2009 through spring 2010, the feature wavelength shortened and by spring 2010 it was only weakly evident.

Overall, the timing of the meander growth from ADT is consistent with geostrophic circulation during the Seaglider surveys and its transition from moderate northward flow to westward flow in spring 2009 as the meander trough was incident on OSP (Figure 20), and near-neutral flow thereafter. Closed contours of a local peak in ADT were centered on the Seaglider survey pattern in autumn 2009-winter 2010, consistent with the reduced incidence of fine structure, weak isopycnal temperature gradients, anticyclonic depth-average vorticity, and near-zero mean circulation observed by Seagliders during this time. Prior to this, one Argo float made a single anticyclonic loop centered at 50°35′N, 144°48′W during spring-summer 2009 before being advected to the northeast (Figures 20e and 20f, Float ID 4901073, labeled "A").

Observations of halocline temperature (θ along $\sigma_\theta = 26.5$ kg m^{-3}) from the Argo array, the CCGS *Tully* along Line P, and Seaglider surveys support the idea that the meander occurred along a water mass front separating cool, fresh Alaska Gyre water to the north and west of OSP from warm and saline waters of the subarctic-subtropical transitional domain, including WSW, to the south and east (Figure 20). The axis of this front appeared to directly overlie the survey pattern in winter 2009, coincident with the maximum strength of eastward temperature gradients along $\sigma_\theta = 26.5$ kg m^{-3} in Seaglider surveys (*cf.* Figure 16). Temperature along this isopycnal decreased near OSP thereafter, as indicated by both Argo floats and Seaglider surveys, suggestive of advection or lateral mixing and spreading within the meander.

The spatial patterns of Argo samples, and their frequent alignment with contours of sea surface dynamic topography, indicate that many floats qualitatively tracked the surface circulation at their inter-profile parking depth (typically 1000 dbar), consistent with the weakly vertically sheared flow observed during Seaglider surveys. Several floats traveled along the NPC meander (e.g., Figures 20c–20e), including one float
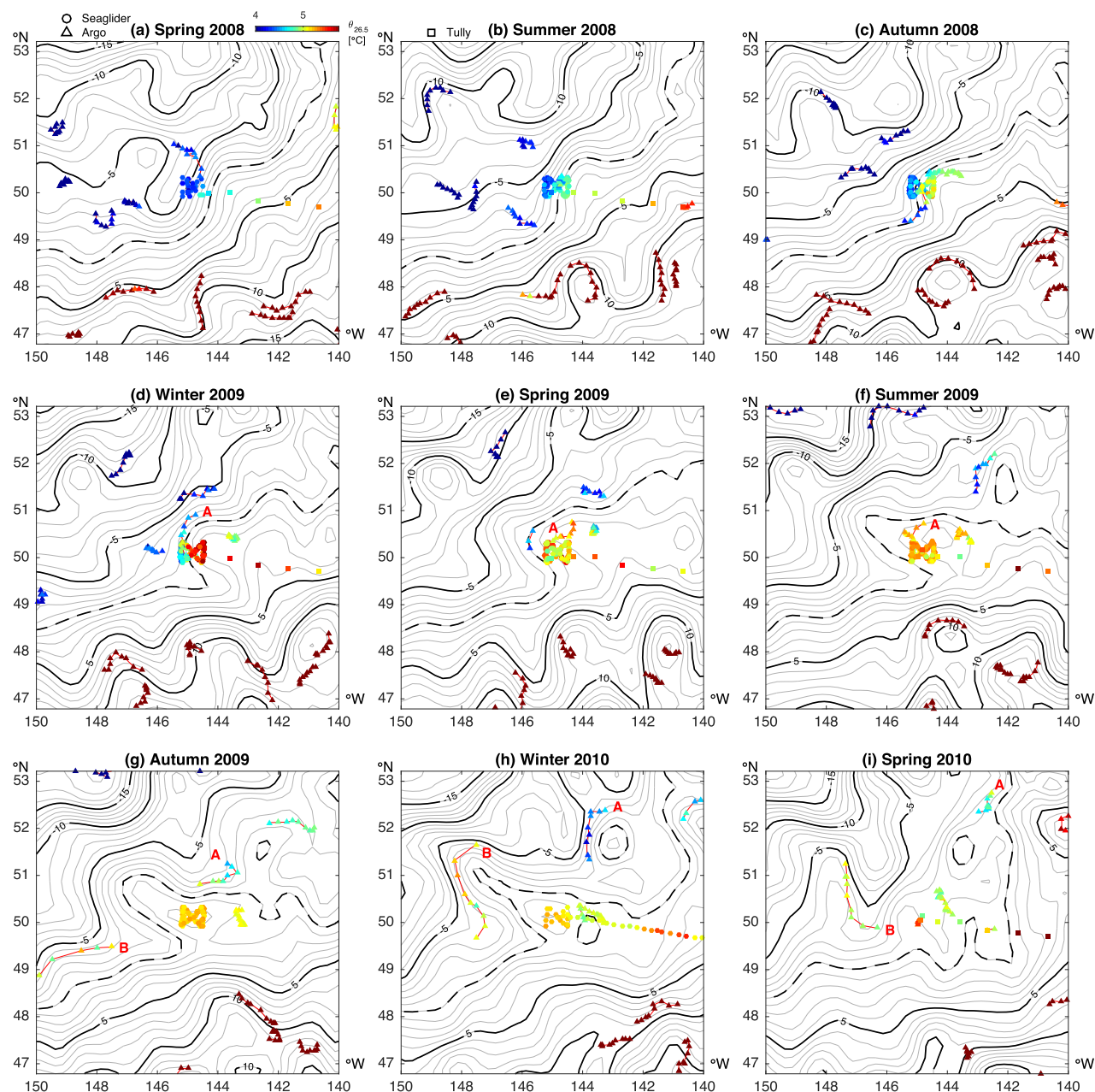
Figure 20. North Pacific Current evolution near Ocean Station Papa, 2008–2010. Plots show Seaglider/Argo/*Tully* observations of potential temperature on $\sigma_\theta = 26.5$ kg m^{-3} (colored circles/triangles/squares, respectively, scale above Figure 20a, values outside range are saturated) in seasonal intervals, overlaid on seasonal averages of AVISO Absolute Dynamic Topography (ADT) sea surface height (gray/black contours drawn at 1 cm/5 cm intervals, respectively). The spatial mean has been removed from each ADT image. Dashed black line highlights the 0 cm contour. Labels "A/B" refer to Argo floats 4901073/2900549, respectively.

that traveled along the complete meander wavelength in autumn 2009-spring 2010 (Float ID 2900549, labeled "B" in Figures 20g–20i). This float sampled halocline temperatures consistent with the warm mode along the meander crest near 51°N, 148°W throughout winter and spring 2010, near where cool mode temperatures had been observed in spring 2008-winter 2009 (compare Figures 20h and 20i with Figures 20a and 20b).

Based on the consistency between various platforms in their descriptions of mesoscale flow and water mass properties, a reasonable conclusion is that a meander in a branch of NPC flow resulted in displacement of its associated water mass front, allowing WSW on the southeast side of the front to reach OSP. The specific dynamical mechanisms surrounding this meander are not explored here, though its growth and

corresponding water mass transport are suggestive of baroclinic instability. Similar wave-like perturbations have been reported previously in the NPC; these were originally attributed to stable, long baroclinic Rossby waves [*Roden*, 1977b; *White*, 1982]. Later studies indicated that the North Pacific Current has both stable and unstable Rossby wave modes, with a decrease in stability if the mean flow has a meridional component, as is the case here [*Kang and Magaard*, 1979; *Kang et al.*, 1982; *Lee and Niiler*, 1987].

5. Conclusions

The consistency between circulation estimates made by Seagliders and two independent platforms—moored ADCPs, and AVISO ADT products—confirms that fortnightly surveys adequately resolved monthly scale mesoscale gradients and flow at OSP. Results here suggest that ongoing OOI mooring-glider time series in this location should be able to resolve mesoscale variability comparably.

The repeat surveys revealed circulation departures over the 18 month observation period that locally overwhelmed the climatological mean flow of the southeastern subpolar gyre. The flow anomalies were accompanied by a shift from relatively cool and fresh Alaska Gyre water to warm, saline, oxygen-rich WSW water in the halocline, and appearance of thermohaline fine structure. These flow and property distortions were due to an anticyclonic meander developing within northeastward NPC flow along a front separating Alaska Gyre water from WSW water to the south and east. While the GOA is a low eddy energy region, eddy flows are sufficient to locally alter circulation on time scales of order a year.

While large, energetic eddies generated along the North American coastal boundary have previously been found to cause abrupt water mass changes at OSP, the repeat survey observations presented here demonstrate an additional mechanism for such changes, due to meandering of the frontal boundary between the subarctic and subtropical gyres. It is likely that future prolonged autonomous observations at OSP will obtain additional realizations of both phenomena.

References

Alford, M., M. Cronin, and J. Klymak (2012), Annual cycle and depth penetration of wind-generated near-inertial internal waves at Ocean Station Papa in the northeast Pacific, *J. Phys. Oceanogr.*, *42*(6), 889–909.

Alford, M., J. MacKinnon, H. Simmons, and J. Nash (2016), Near-inertial internal gravity waves in the ocean, *Annu. Rev. Mar. Sci.*, *8*, 95–123, doi:10.1146/annurev-marine-010814-015746.

Archer, D., S. Emerson, T. Powell, and C. Wong (1993), Numerical hindcasting of sea surface pCO₂ at Weathership Ocean Station Papa, *Prog. Oceanogr.*, *32*, 319–351.

Aydin, M., Z. Top, R. Fine, and D. Olson (1998), Modification of intermediate waters in the northeastern subpolar Pacific, *J. Geophys. Res.*, *103*(C13), 30,923–30,940.

Aydin, M., Z. Top, and D. Olson (2004), Exchange processes and watermass modifications along the subarctic front in the North Pacific: Oxygen consumption rates and net carbon flux, *J. Mar. Res.*, *62*, 153–167.

Boyer, T., et al. (2013), World Ocean Database 2013, in *NOAA Atlas NESDIS 72*, edited by S. Levitus and A. Mishonov, 209 pp., NOAA, Silver Spring, Md., doi:10.7289/V5NZ85MT.

Bretherton, C. S., M. Widmann, V. P. Dymnikov, J. M. Wallace, and I. Bladé (1999), The effective number of spatial degrees of freedom of a time-varying field, *J. Clim.*, *12*, 1990–2009.

Castro, C., F. Chavez, and C. Collins (2001), Role of the California Undercurrent in the export of denitrified waters from the eastern tropical North Pacific, *Global Biogeochem. Cycles*, *15*(4), 819–830.

Chelton, D., M. Schlax, and R. Samelson (2011), Global observations of nonlinear mesoscale eddies, *Prog. Oceanogr.*, *91*, 167–216.

Crawford, W., P. Brickley, and A. Thomas (2007), Mesoscale eddies dominate surface phytoplankton in northern Gulf of Alaska, *Prog. Oceanogr.*, *75*, 287–303.

Crawford, W. R., P. J. Brickley, T. D. Peterson, and A. C. Thomas (2005), Impact of Haida eddies on chlorophyll distribution in the eastern Gulf of Alaska, *Deep Sea Res., Part II*, *52*, 975–989.

Cronin, M., R. Weller, S. Lampitt, and U. Send (2012), Ocean reference stations, in *Earth Observation*, edited by R. Rustamov and S. Salahova, pp. 203–228, InTech, Rijeka, Croatia. [Available at http://www.intechopen.com/books/earth-observation/ocean-reference-stations.]

Cronin, M., N. Pelland, W. Crawford, and S. Emerson (2015), Estimating diffusivity from the mixed layer heat and salt balances in the North Pacific, *J. Geophys. Res. Oceans*, *120*, 7346–7362, doi:10.1002/2015JC011010.

Crosby, D., L. Breaker, and W. Gemmill (1993), A proposed definition for vector correlation in geophysics: Theory and application, *J. Atmos. Oceanic Technol.*, *10*, 355–367.

Cummins, P., and H. Freeland (2007), Variability of the North Pacific Current and its bifurcation, *Prog. Oceanogr.*, *75*, 253–265.

Cummins, P., and G. Lagerloef (2002), Low-frequency pycnocline depth variability at ocean weather station P in the Northeast Pacific, *J. Phys. Oceanogr.*, *32*, 3207–3215.

Damerell, G. M., K. J. Heywood, A. F. Thompson, U. Binetti, and J. Kaiser (2016), The vertical structure of upper ocean variability at the Porcupine Abyssal Plain during 2012-2013, *J. Geophys. Res. Oceans*, *121*, 3075–3089, doi:10.1002/2015JC011423.

D'Asaro, E. (1985), Upper ocean temperature structure, inertial currents, and Richardson numbers observed during strong meteorological forcing, *J. Phys. Oceanogr.*, *15*, 943–962.

D'Asaro, E., C. Eriksen, M. Levine, P. Niiler, C. Paulson, and P. van Meurs (1995), Upper-ocean inertial currents forced by a strong storm. Part I: Data and comparisons with linear theory, *J. Phys. Oceanogr.*, *25*, 2909–2936.

Davis, R., R. deSzoeke, D. Halpern, and P. Niiler (1981a), Variability in the upper ocean during MILE. Part I: The heat and momentum balances, *Deep Sea Res., Part A*, 28(12), 1427–1451.

Davis, R., R. deSzoeke, and P. Niiler (1981b), Variability in the upper ocean during MILE. Part II: Modeling the mixed layer response, *Deep Sea Res., Part A*, 28, 1453–1475.

Denman, K., and M. Miyake (1973), Upper layer modification at Ocean Station Papa: Observations and simulation, *J. Phys. Oceanogr.*, 3(2), 185–196.

Dodimead, A., F. Favorite, and T. Hirano (1963), Salmon of the North Pacific Ocean, Part II: Review of oceanography of the Subarctic Pacific region, *Bull. 13*, Int. North Pac. Fish. Comm., Vancouver, British Columbia, Canada.

Dohan, K., and R. Davis (2011), Mixing in the transition layer during two storm events, *J. Phys. Oceanogr.*, 41, 42–66.

Emerson, S. (1987), Seasonal oxygen cycles and biological new production in surface waters of the subarctic Pacific Ocean, *J. Geophys. Res.*, 92(C6), 6535–6544.

Emerson, S., and C. Stump (2010), Net biological oxygen production in the ocean—II: Remote *in situ* measurements of O_2 and N_2 in subarctic Pacific surface waters, *Deep Sea Res., Part I*, 57, 1255–1265.

Emerson, S., C. Stump, and D. Nicholson (2008), Net biological oxygen production in the ocean: Remote *in situ* measurements of O_2 and N_2 in surface waters, *Global Biogeochem. Cycles*, 22, GB3023, doi:10.1029/2007GB003095.

Emerson, S., C. Sabine, M. Cronin, R. Feely, S. Cullison, and M. DeGrandpre (2011), Quantifying the flux of $CaCO_3$ and organic carbon from the surface ocean using *in situ* measurements of O_2, N_2, pCO_2 and pH, *Global Biogeochem. Cycles*, 25, GB3008, doi:10.1029/2010GB003924.

Eriksen, C., T. Osse, R. Light, T. Wen, T. Lehman, P. Sabin, J. Ballard, and A. Chiodi (2001), Seaglider: A long-range autonomous underwater vehicle for oceanographic research, *IEEE J. Oceanic Eng.*, 26(4), 424–436.

Fassbender, A. J., C. L. Sabine, and Cronin M. F. (2016), Net community production and calcification from 7 years of NOAA Station Papa Mooring measurements. *Global Biogeochem. Cycles* 30(2), 250–267, doi:10.1002/2015GB005205.

Favorite, F., A. J. Dodimead, and K. Nasu (1976), Oceanography of the Subarctic Pacific region, 1960-71, *Bull. 33*, Int. North Pac. Fish. Comm., Vancouver, British Columbia, Canada.

Flament, P. (2002), A state variable for characterizing water masses and their diffusive stability: Spiciness, *Prog. Oceanogr.*, 54, 493–501.

Freeland, H. (2007), A short history of Ocean Station Papa and Line P, *Prog. Oceanogr.*, 75, 120–125.

Freeland, H. (2013), Vertical velocity estimates in the North Pacific using Argo floats, *Deep Sea Res., Part II*, 85, 75–80.

Freeland, H., and P. Cummins (2005), Argo: A new tool for environmental monitoring and assessment of the world's oceans, an example from the N.E. Pacific, *Prog. Oceanogr.*, 64, 31–44.

Freeland, H., K. Denman, C. Wong, F. Whitney, and R. Jacques (1997), Evidence of change in the winter mixed layer in the Northeast Pacific Ocean, *Deep Sea Res., Part I*, 44(12), 2117–2129.

Freeland, H., G. Gatien, A. Huyer, and R. Smith (2003), Cold halocline in the northern California Current: An invasion of subarctic water, *Geophys. Res. Lett.*, 30(3), 1141, doi:10.1029/2002GL016663.

Gaspar, P. (1988), Modeling the seasonal cycle of the upper ocean, *J. Phys. Oceanogr.*, 18, 161–180.

Gill, A. (1974), The stability of planetary waves on an infinite beta-plane, *Geophys. Astrophys. Fluid Dyn.*, 6, 29–47.

Hamme, R., et al. (2010), Volcanic ash fuels anomalous plankton bloom in subarctic northeast Pacific, *Geophys. Res. Lett.*, 37, L19604, doi:10.1029/2010GL044629.

Holton, J. R. (1992), *An Introduction to Dynamic Meteorology*, 3rd ed., 507 pp., Academic Press, San Diego, Calif.

Jackson, J., P. Myers, and D. Ianson (2009), An examination of mixed layer sensitivity in the Northeast Pacific Ocean from July 2001-July 2005 using the general ocean turbulence model and Argo data, *Atmos. Ocean*, 47(2), 139–153.

Johnson, G., S. Schmidtko, and J. Lyman (2012), Relative contributions of temperature and salinity to seasonal mixed layer density changes and horizontal density gradients, *J. Geophys. Res.*, 117, C04015, doi:10.1029/2011JC007651.

Kalnay, E., et al. (1996), The NCEP/NCAR 40-year reanalysis project, *Bull. Am. Meteorol. Soc.*, 77(3), 437–471.

Kang, Y. Q., and L. Magaard (1979), Stable and unstable Rossby waves in the North Pacific Current as inferred from the mean stratification, *Dyn. Atmos. Oceans*, 3(1), 1–14.

Kang, Y. Q., J. M. Price, and L. Magaard (1982), On stable and unstable Rossby waves in non-zonal oceanic shear flow, *J. Phys. Oceanogr.*, 12, 528–537.

Klymak, J. M., W. Crawford, M. H. Alford, J. A. MacKinnon, and R. Pinkel (2015), Along-isopycnal variability of spice in the North Pacific, *J. Geophys. Res. Oceans*, 120, 2287–2307, doi:10.1002/2013JC009421.

Koopmans, L. H. (1974), *The Spectral Analysis of Time Series*, 366 pp., Academic Press, N. Y.

Kunze, E. (1985), Near-inertial wave propagation in geostrophic shear, *J. Phys. Oceanogr.*, 15, 544–565.

Large, W. (1996), An observational and numerical investigation of the climatological heat and salt balances at OWS Papa, *J. Clim.*, 9, 1856–1876.

Large, W., and G. Crawford (1995), Observations and simulations of upper-ocean response to wind events during the ocean storms experiment, *J. Phys. Oceanogr.*, 25, 2831–2852.

Large, W., J. McWilliams, and P. Niiler (1986), Upper ocean thermal response to strong autumnal forcing of the Northeast Pacific, *J. Phys. Oceanogr.*, 16, 1524–1550.

Large, W., J. McWilliams, and S. Doney (1994), Oceanic vertical mixing: A review and a model with a nonlocal boundary layer parameterization, *Rev. Geophys.*, 32, 363–403.

Lee, D.-K., and P. Niiler (1987), The local baroclinic instability of geostrophic spirals in the Eastern North Pacific, *J. Phys. Oceanogr.*, 17, 1366–1377.

Li, M., P. Myers, and H. Freeland (2005), An examination of historical mixed layer depths along Line P in the Gulf of Alaska, *Geophys. Res. Lett.*, 32, L05613, doi:10.1029/2004GL021911.

Lyman, J., and G. Johnson (2015), Anomalous eddy heat and freshwater transport in the Gulf of Alaska, *J. Geophys. Res. Oceans*, 120, 1397–1408, doi:10.1002/2014JC010252.

Lynn, R. J. (1986), The Subarctic and Northern Subtropical Fronts in the Eastern North Pacific Ocean in spring, *J. Phys. Oceanogr.*, 16, 209–222.

Martin, P. (1985), Simulation of the mixed layer at OWS November and Papa with several models, *J. Geophys. Res.*, 90(C1), 903–916.

Matear, R. (1993), Circulation within the ocean storms area located in the Northeast Pacific Ocean determined by inverse methods, *J. Phys. Oceanogr.*, 23, 648–658.

McClain, C., K. Arrigo, K.-S. Tai, and D. Turk (1996), Observations and simulations of physical and biological processes at ocean weather station P, 1951-1980, *J. Geophys. Res.*, 101(C2), 3697–3713.

McWilliams, J. C. (2006), *Fundamentals of Geophysical Fluid Dynamics*, 249 pp., Cambridge Univ. Press, N. Y.

Nicholson, D., S. Emerson, and C. Eriksen (2008), Net community production in the deep euphotic zone of the subtropical North Pacific gyre from glider surveys, *Limnol. Oceanogr.*, *53(5)*, 2226–2236.

Paduan, J., and R. deSzoeke (1986), Heat and energy balances in the upper ocean at 50°N, 140°W during November 1980 (STREX), *J. Phys. Oceanogr.*, *16*, 25–38.

Paduan, J., and P. Niiler (1993), Structure of velocity and temperature in the Northeast Pacific as measured with Lagrangian drifters in fall 1987, *J. Phys. Oceanogr.*, *23*, 585–600.

Pelland, N. (2015), Eddy circulation, heat and salt balances, and ocean metabolism: Observations from a Seaglider-Mooring array at Ocean Station Papa, PhD thesis, Univ. of Wash., Seattle. [Available at http://hdl.handle.net/1773/35285.]

Pelland, N., C. Eriksen, and C. Lee (2013), Subthermocline eddies over the Washington continental slope as observed by Seagliders, 2003-09, *J. Phys. Oceanogr.*, *43*, 2025–2053.

Ren, L., and S. Riser (2009), Seasonal salt budget in the northeast Pacific Ocean, *J. Geophys. Res.*, *114*, C12004, doi:10.1029/2009JC005307.

Rio, M.-H., S. Mulet, E. Greiner, N. Picot, and A. Pascual (2013), New global Mean Dynamic Topography from a GOCE geoid model, altimeter measurements and oceanographic *in situ* data, paper presented at OSTST 2013 Meeting, Boulder Colo., AVISO Altimetry, Ramonville St Agne, France. [Available at http://www.aviso.altimetry.fr/fileadmin/documents/OSTST/2013/oral/mulet_MDT_CNES_CLS13.pdf.]

Robinson, A., and J. McWilliams (1974), The Baroclinic instability of the open ocean, *J. Phys. Oceanogr.*, *4(3)*, 281–294.

Roden, G. (1977a), Oceanic Subarctic Fronts of the Central Pacific: Structure of and response to atmospheric forcing, *J. Phys. Oceanogr.*, *7*(6), 761–778.

Roden, G. (1977b), On long-wave disturbances of dynamic height in the North Pacific, *J. Phys. Oceanogr.*, *7*, 41–49.

Roden, G. (1991), Subarctic-Subtropical Transition Zone of the North Pacific: Large-scale aspects and mesoscale structure, in *Biology, Oceanography, and Fisheries of the North Pacific Transition Zone and Subarctic Frontal Zone, NOAA Tech. Rep. NMFS 105*, pp. 1–38, NMFS Scientific Publications Office, Seattle, Wash., [Available at http://spo.nwr.noaa.gov/tr105.pdf.]

Ruddick, B., and K. Richards (2003), Oceanic thermohaline intrusions: Observations, *Prog. Oceanogr.*, *56*, 499–527.

Rudnick, D., and S. Cole (2011), On sampling the ocean using underwater gliders, *J. Geophys. Res.*, *116*, C08010, doi:10.1029/2010JC006849.

Shcherbina, A., M. Gregg, M. Alford, and R. Harcourt (2009), Characterizing thermohaline intrusions in the North Pacific Subtropical Frontal Zone, *J. Phys. Oceanogr.*, *39*, 2735–2756.

SSALTO/DUACS (2015), *User Handbook: (M)SLA and (M)ADT Near-Real Time and Delayed Time Products*, Issue 4 rev. 2, 60 pp., AVISO Altimetry, Ramonville St Agne, France. [Available at http://www.aviso.altimetry.fr/fileadmin/documents/data/tools/hdbk_duacs.pdf.]

Steiner, N., S. Vagle, K. Kenman, and C. McNeil (2007), Oxygen and nitrogen cycling in the northeast Pacific—Simulations and observations at Station Papa in 2003/2004, *J. Mar. Res.*, *65*, 441–469.

Sydeman, W., S. Thompson, J. Field, W. Peterson, R. Tanasichuk, H. Freeland, S. Bograd, and R. Rykaczewski (2011), Does positioning of the North Pacific Current affect downstream ecosystem productivity?, *Geophys. Res. Lett.*, *38*, L12606, doi:10.1029/2011GL047212.

Tabata, S. (1965), Variability of oceanic conditions at Station "P" in the Northeast Pacific Ocean, *Trans. R. Soc. Can.*, *4*, 367–478.

Tabata, S., and L. F. Giovando (1963), The Seasonal Thermocline at Ocean Weather Station "P" During 1956 Through 1959, *Manuscr. Rep. Ser., Oceanogr. and Limnol.*, *157*, Fish. Res. Board of Can, Nanaimo, British Columbia, Canada. [Available at http://www.dfo-mpo.gc.ca/Library/52200.pdf.]

Taguchi, B., N. Schneider, and M. Nonaka (2015), Decadal variability of upper ocean heat content in the western boundary currents regions, Int. Union Geod. Geophys. Gen. Assem., Abstract IUGG-2888. [Available at: http://www.czech-in.org/cmdownload/IUGG2015/presentations/IUGG-2888.pdf.]

Thomas, F., V. Garcon, and J.-F. Minster (1990), Modelling the seasonal cycle of dissolved oxygen in the upper ocean at Ocean Weather Station P, *Deep Sea Res., Part A*, *37*(3), 463–491.

Thompson, A. F., A. Lazar, C. Buckingham, A. C. Naveira Garabato, G. Damerell, and K. Heywood (2016), Open-ocean submesoscale motions: A full seasonal cycle of mixed layer instabilities from gliders, *J. Phys. Oceanogr.*, *46*, 1285–1307.

Thomson, J., E. D'Asaro, M. Cronin, W. Rogers, R. Harcourt, and A. Shcherbina (2013), Waves and the equilibrium range at Ocean Weather Station P, *J. Geophys. Res. Oceans*, *118*, 5951–5962, doi:10.1002/2013JC008837.

Thomson, R., and I. Fine (2009), A diagnostic model for mixed layer depth estimation with application to Ocean Station P in the Northeast Pacific, *J. Phys. Oceanogr.*, *39*, 1399–1415.

Thomson, R., and M. Krassovski (2010), Poleward reach of the California Undercurrent extension, *J. Geophys. Res.*, *115*, C09027, doi:10.1029/2010JC006280.

Thomson, R., P. LeBlond, and W. Emery (1990), Analysis of deep-drogued satellite-tracked drifter measurements in the Northeast Pacific, *Atmos. Ocean*, *28*(4), 409–443.

Torruella, A. (1995), The fall upper ocean heat balance in the Northeast Pacific, PhD thesis, Scripps Inst. of Oceanogr., San Diego, Calif.

Tully, J., A. Dodimead, and S. Tabata (1960), An anomalous increase of temperature in the ocean off the pacific coast of Canada through 1957 and 1958, *J. Fish. Res. Board Can.*, *17*(1), 61–80.

Vagle, S., C. McNeil, and N. Steiner (2010), Upper ocean bubble measurements from the NE Pacific and estimates of their role in air-sea gas transfer of the weakly soluble gases nitrogen and oxygen, *J. Geophys. Res.*, *115*, C12,054, doi:10.1029/2009JC005990.

White, W. (1982), Traveling wave-like mesoscale perturbations in the North Pacific Current, *J. Phys. Oceanogr.*, *12*, 231–243.

Whitney, F., and H. Freeland (1999), Variability in upper-ocean water properties in the NE Pacific Ocean, *Deep Sea Res., Part II*, *46*, 2351–2370.

Whitney, F., H. Freeland, and M. Robert (2007), Persistently declining oxygen levels in the interior waters of the eastern subarctic Pacific, *Prog. Oceanogr.*, *75*, 179–199.

Wong, C., N. Waser, Y. Nojiri, F. Whitney, J. Page, and J. Zeng (2002), Seasonal cycles of nutrients and dissolved inorganic carbon at high and mid latitudes in the North Pacific Ocean during the *Skaugran* cruises: Determination of new production and nutrient uptake ratios, *Deep Sea Res., Part II*, *49*, 5317–5338.

Wu, C. (1986), Jackknife, bootstrap, and other resampling methods in regression analysis, *Ann. Stat.*, *14*(4), 1261–1295.

Yuan, X., and L. Talley (1996), The subarctic frontal zone in the North Pacific: Characteristics of frontal structure from climatological data and synoptic surveys, *J. Geophys. Res.*, *101*(C7), 16,491–16,508.